npj | computational materials

Article

Published in partnership with the Shanghai Institute of Ceramics of the Chinese Academy of Sciences

https://doi.org/10.1038/s41524-026-02141-7

Rigid muffin-tin approximation in plane-wave codes for fast modeling of phonon-mediated superconductors

Danylo Radevych[1] ✉, Tatsuya Shishidou[2], Michael Weinert[2], Elena R. Margine[3], Aleksey N. Kolmogorov[3] & Igor I. Mazin[1,4]

We present a pseudopotential-based plane-wave implementation of the rigid muffin-tin approximation (RMTA), offering a computationally efficient alternative to its traditional use in all-electron codes. The RMTA partitions the total electron-phonon coupling constant into a sum of local atomic contributions, each defined as the product of electronic and ionic factors. The former is represented by McMillan–Hopfield parameters derived from angular-momentum-resolved electron-phonon matrix elements, while the latter can be obtained from the local force matrix. Here, we derive and incorporate the electronic part of the RMTA within the widely used pseudopotential framework. We show that the McMillan–Hopfield parameters for elemental transition metals and their compounds are in excellent agreement with the results of full-potential linearized augmented plane wave calculations. Furthermore, we formulate scalable strategies for computing the ionic factors and estimate the full electron-phonon coupling constant and critical temperature. Integration of RMTA descriptors into high-throughput workflows opens a cost-effective route for screening candidate superconductors.

Historically, the first practical method for calculating the electron-phonon coupling (EPC) constant in metals was the rigid muffin-tin approximation (RMTA)[1–3], in which the electronic potential within a sphere around each atom, called a muffin-tin (MT) sphere, was assumed to follow ionic displacements rigidly. Since the RMTA was formulated in terms of MT potentials and wavefunctions expanded in radial functions and spherical harmonics, it was naturally implemented in many all-electron approaches, such as the augmented plane wave (APW)[4–8], Korringa–Kohn–Rostoker (KKR)[9–11], and linear muffin-tin orbital (LMTO)[6,12,13] methods, where atomic functions inside the MT sphere are evaluated explicitly. The RMTA worked reasonably well for the elements with localized *d*-orbitals in close-packed structures (e.g., V, Nb, Mo, and Pd)[12,14–20]. It was used to calculate the phonon-limited electrical resistivity in metals[18] and to study superconductivity in $A15$[16,21,22] and $C15$[23] compounds, hydrides[24–27], nitrides[28,29], carbides[4,28], perovskites[30,31], and other materials[32–37]. While this method was designed with transition metals in mind, and routinely tended to underestimate the EPC in *sp*-metals, corrections accounting for the long-range tails of the ionic MT potential in such materials have been proposed[19,38] and successfully applied to, e.g., Ag[19], and Al, Ga, and Pb[38].

Later on, the RMTA was superseded by the significantly more accurate and universal linear-response method, formulated within density-functional perturbation theory (DFPT)[39–42], and by superconducting density-functional theory (SCDFT)[43–46]. Both frameworks are well-suited for efficient pseudopotential-based plane-wave (PP+PW) codes and are widely employed to predict superconducting properties. While the first high-throughput materials screenings involving thousands of superconductivity calculations based on the Eliashberg spectral function (α^2F) have been recently reported[47–52], the substantial computational cost of DFPT continues to impose limitations in the form of restricted unit cell sizes or confined composition spaces. Although these efforts mark important milestones in applying machine learning for superconductor discovery, larger datasets, producible with fast physics-based methods, are necessary to identify broader design rules.

Several fast descriptors for superconductors have been proposed, typically tailored to specific material families. For MgB_2-type layered compounds, the frequency difference between in-plane boron phonons at the M and Γ points was used as a softening marker expected to correlate with the EPC[53]. In *sp*-metals, scaled EPC constants evaluated at the Brillouin-zone center were introduced as a proxy for the total EPC[54,55], but this approach cannot describe cases where zone-boundary phonons play a significant role. More recently, finite-displacement calculations at a small number of high-symmetry *q*-points combined with energy band shifts were

[1]Department of Physics and Astronomy, George Mason University, Fairfax, VA, USA. [2]Department of Physics, University of Wisconsin-Milwaukee, Milwaukee, WI, USA. [3]Department of Physics, Applied Physics and Astronomy, Binghamton University-SUNY, Binghamton, NY, USA. [4]Quantum Science and Engineering Center, George Mason University, Fairfax, VA, USA. ✉e-mail: dradevyc@gmu.edu

proposed to estimate the EPC across materials of general chemistry, with particular emphasis on phases with large unit cells[56], although to date the method has been applied exclusively to *sp*-bonded metals and hydrides. Real-space descriptors have also been explored, including the electron-localization function[57,58] and spatial derivatives of the Kohn–Sham potential[59], which were used to estimate the critical temperature (T_c) in hydrogen-based superconductors. While effective within their target classes, usually comprising light elements, these descriptors underscore the need for approaches that can be extended to transition metals and their compounds. The RMTA could address this problem, but so far it has not been formulated in a way suitable for pseudopotential-based codes, which are preferably used by modern search algorithms. In this work, the RMTA EPC constant is reformulated for such platforms through its partitioning into electronic and ionic factors. This ionic, rather than phonon, representation can be viewed as Eliashberg theory written in terms of ion-displacement Green functions[17,60].

The method developed for the electronic factor, which is a fast but non-trivial postprocessing step on top of a standard self-consistent field (SCF) density-functional theory (DFT) calculation, is applied to transition metals and their compounds. The corresponding electron-phonon (EP) matrix elements[12] and McMillan–Hopfield (MH) parameters[3,12,17,61,62] calculated with this method are shown to agree well with the RMTA implementation within the full-potential linearized augmented plane wave (FLAPW) method. The ionic factor is evaluated in terms of the local blocks of the interatomic force constant (IFC) matrix, which can be extracted from finite-displacement supercell calculations at a negligible computational cost using universal machine learning potentials (uMLPs). Comprehensive benchmark studies have established the effectiveness of these interatomic models for the analysis of vibrational properties[63,64]. The equivariant Smooth Energy Network (eSEN)[65] used in this study is ranked among the most accurate architectures[66]. Ionic factors obtained using this approach are shown to be in excellent agreement with their ab initio counterparts; the latter remain the robust moderate-cost option in cases where pre-trained uMLPs lack the necessary accuracy for the target systems[66].

Results

The primary results presented here are the methodology developed for RMTA calculations within the PP + PW framework and the quantitative verification of this method for benchmark materials. This Section describes the three assumptions underlying the RMTA[36,67], including the definitions of the electronic and ionic factors for atom- and type-resolved EPC constants. Furthermore, formulations compatible with PP+PW codes are provided, and results are compared to reference values obtained via other computational methods. Unless stated otherwise, Rydberg atomic units are assumed throughout the equations.

Assumption 1: rigid-ion approximation

The RMTA relies on the assumption that a change in the potential acting on an electron located at $\boldsymbol{r}$ relative to the ionic center $\boldsymbol{\tau}_\kappa$ arises from a rigid displacement of the electron-ion interaction potential $V_\kappa(\boldsymbol{r})$ (see Fig. 1), so that it is given by the dot product of the ionic displacement $\Delta\boldsymbol{\tau}_\kappa$ and the potential gradient ∇V_κ. In the present work, this change is evaluated through Eq. (1) using the spherical part of the potential, $V_\kappa(r)$, following the original RMTA formulations[1,2,12].

$$\Delta V_\kappa(r) \approx -\Delta\boldsymbol{\tau}_\kappa \cdot \nabla V_\kappa(r) = -\left(\Delta\boldsymbol{\tau}_\kappa \cdot \hat{\boldsymbol{r}}\right)\frac{dV_\kappa(r)}{dr}. \tag{1}$$

Assumption 2: local-vibration approximation

In the RMTA, the EP interaction is treated as local in real space[1,3], such that the total EPC constant for the whole material, λ, can be represented as a sum

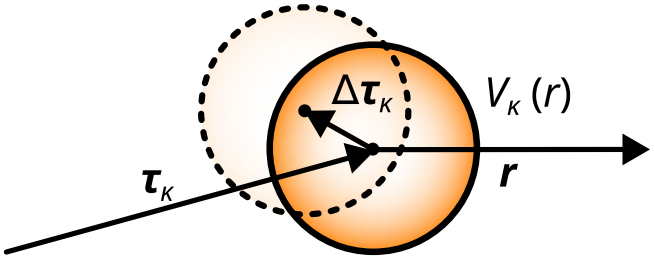

Fig. 1 | Vector definitions for the rigid-ion approximation. The schematic illustrates the relationship among the ionic center $\boldsymbol{\tau}_\kappa$, the electron position $\boldsymbol{r}$, and the displacement vector $\Delta\boldsymbol{\tau}_\kappa$, which are used to evaluate the potential change in Eq. (1).

of atomic EPC constants $\widetilde{\lambda}_\kappa$ over N_{atoms} atoms in the considered cell[25,68]:

$$\lambda = \sum_{\kappa}^{N_{\text{atoms}}} \widetilde{\lambda}_\kappa. \tag{2}$$

The EPC constant for each atom can be written[17,32] in terms of the full IFC matrix, Φ, as

$$\widetilde{\lambda}_\kappa = \sum_{\alpha\beta} \widetilde{\eta}_{\kappa,\alpha\beta}\left[\Phi^{-1}\right]_{\kappa\alpha\boldsymbol{0},\kappa\beta\boldsymbol{0}}, \tag{3}$$

where α and β are Cartesian indices, and $\boldsymbol{0}$ are coordinates of the original unit cell. In the rigid-ion approximation, the electronic tensor $\widetilde{\eta}_{\kappa,\alpha\beta}$ is substituted by its isotropic average defined by the MH parameter $\widetilde{\eta}_\kappa$,

$$\widetilde{\eta}_\kappa = \sum_{\alpha\beta} \widetilde{\eta}_{\kappa,\alpha\beta}\delta_{\alpha\beta}, \tag{4}$$

$$\widetilde{\eta}_{\kappa,\alpha\beta} \approx \frac{1}{3}\widetilde{\eta}_\kappa\delta_{\alpha\beta}. \tag{5}$$

The non-local phonon contribution in Eq. (3) is further approximated by the local lattice response, such that the EPC constant takes the form[3,17,69]:

$$\widetilde{\lambda}_\kappa \approx \widetilde{\eta}_\kappa\left(\frac{1}{3}\mathrm{Tr}\left[\left(\Phi_{\kappa\kappa}\right)^{-1}\right]\right) = \widetilde{\eta}_\kappa\widetilde{\phi}_\kappa. \tag{6}$$

Here, $\widetilde{\eta}_\kappa$ and $\widetilde{\phi}_\kappa$ are the electronic and ionic factors, respectively. In Eq. (6), $\left(\Phi_{\kappa\kappa}\right)^{-1}$ is the inverse of the 3×3 block $\Phi_{\kappa\kappa}$ of Φ corresponding to the cell at $\boldsymbol{0}$, with elements

$$\left[\Phi_{\kappa\kappa}\right]_{\alpha\beta} = \Phi_{\kappa\alpha\boldsymbol{0},\kappa\beta\boldsymbol{0}}. \tag{7}$$

The present approximation for the ionic factor is equivalent to the Einstein solid model[70,71], in which the IFC matrix is assumed to be diagonal in site indices. Traditionally, the lattice response has been written in terms of the averaged eigenvalue of $\left(\Phi_{\kappa\kappa}\right)^{-1}$, $\langle\left[M_\kappa\omega_\kappa^2\right]^{-1}\rangle$,

$$\widetilde{\phi}_\kappa = \left\langle\frac{1}{M_\kappa\omega_\kappa^2}\right\rangle \approx \frac{1}{M_\kappa\langle\omega_\kappa^2\rangle}, \tag{8}$$

where M_κ and ω_κ are the atomic mass and characteristic phonon frequency, respectively. The last part of Eq. (8), which is an approximation of $\widetilde{\phi}_\kappa$ defined in Eq. (6), was interpreted as the inverse of the effective local stiffness and, in simple metals, further approximated using the experimental Debye temperature, θ_D, via the relation $\langle\omega_\kappa^2\rangle \approx \frac{1}{2}\theta_D^2$[3,14,17,61,62].

The derivation of the analytical expressions for the electronic factor is substantially more involved, given their direct dependence on pseudopotentials (PPs) and the associated atomic functions. The corresponding atomic MH parameter, $\widetilde{\eta}_\kappa$, is defined as the Fermi-surface average of the

squared EP matrix elements for states at the Fermi level, divided by the electronic density of states (eDOS) $N(\varepsilon_F)$ at the Fermi energy ε_F:

$$\widetilde{\eta}_\kappa = \frac{\Omega^2}{(2\pi)^6 N(\varepsilon_F)} \sum_{ij}^{N_{\text{states}}} \int_{\text{BZ}} d\boldsymbol{k}\delta\left(\varepsilon_{i,\boldsymbol{k}} - \varepsilon_F\right) \int_{\text{BZ}} d\boldsymbol{k}'\delta\left(\varepsilon_{j,\boldsymbol{k}'} - \varepsilon_F\right) \times \left|\left\langle \Psi_{j,\boldsymbol{k}'} \middle| \nabla V_\kappa(r) \middle| \Psi_{i,\boldsymbol{k}} \right\rangle\right|^2, \tag{9}$$

where $N(\varepsilon_F)$ is defined *per cell per spin*; $\varepsilon_{i,\boldsymbol{k}}$ and $\varepsilon_{j,\boldsymbol{k}'}$ are the Hamiltonian eigenvalues of the states i and j corresponding to the wavefunctions $\Psi_{i,\boldsymbol{k}}(\boldsymbol{r})$ and $\Psi_{j,\boldsymbol{k}'}(\boldsymbol{r})$ at momenta $\boldsymbol{k}$ and $\boldsymbol{k}'$, respectively; N_{states} is the total number of electronic states; Ω is the unit cell volume; and "BZ" marks the integration over the Brillouin zone. The eDOS in the denominator of Eq. (9) makes the atomic MH parameter and the corresponding atomic EPC constant dependent on the cell size. The total EPC constant, λ in Eq. (2), however, is independent of the cell size.

In materials where different Wyckoff positions are occupied, it is convenient to introduce the EPC constant λ_ν for each of the N_{types} symmetry types, as defined in Eq. (10). Each symmetry type includes only atoms of the same chemical element that are related by crystallographic symmetry operations, with N^ν_{atoms} being the number of atoms per type ν. The second equality of Eq. (10) follows from the fact that all atoms belonging to the same type (Wyckoff position) ν share identical values of $\widetilde{\lambda}_\kappa$.

$$\lambda_\nu = \sum_{\kappa\in\{\nu\}}^{N^\nu_{\text{atoms}}} \widetilde{\lambda}_\kappa = N^\nu_{\text{atoms}} \widetilde{\lambda}_\kappa\Big|_{\forall\kappa\in\{\nu\}}. \tag{10}$$

Unlike the atomic EPC constants, the type-specific EPC constants, λ_ν, are independent of the cell size. The total EPC constant is then given by a sum over the EPC constants corresponding to different symmetry types [see Eq. (11)][16,26,30,72,73]. Importantly, the ability to find the contributions of individual symmetry types to the overall EPC in compounds allows for a straightforward comparison between these contributions in different materials.

$$\lambda = \sum_{\nu}^{N_{\text{types}}} \lambda_\nu. \tag{11}$$

Crystallographically equivalent atoms share an identical ionic factor $\widetilde{\phi}_\kappa$. Consequently, the expression for a given symmetry type is

$$\phi_\nu = \widetilde{\phi}_\kappa \,\forall\, \kappa \in \{\nu\}. \tag{12}$$

It follows from Eq. (12) that the MH parameters for different symmetry types can also be introduced as

$$\eta_\nu = N^\nu_{\text{atoms}} \widetilde{\eta}_\kappa \,\forall\, \kappa \in \{\nu\}. \tag{13}$$

Similar to the type-specific EPC constants, the type-specific MH parameters do not depend on the cell size. Although the present formalism uses atomic parameters, only the type-specific ones are reported in the "Quantitative verification" section since they can be compared across different materials regardless of the unit-cell choice.

Assumption 3: spherical-band approximation

The RMTA assumes that, inside the MT sphere of atom κ with radius $r_{\kappa,\text{MT}}$, the wavefunction of state i can be expanded in terms of radial functions $R_{\kappa,l}(r, \varepsilon_{i,\boldsymbol{k}})$ associated with the local screened potential $V_\kappa(r)$ and spherical harmonics $Y_{lm}(\widehat{\boldsymbol{r}})$ labeled by quantum numbers l and m, with momentum-dependent coefficients $a_{i\kappa,lm}(\boldsymbol{k})$:

$$\Psi_{i,\boldsymbol{k}}(\boldsymbol{r}) = \sum_{lm} a_{i\kappa,lm}(\boldsymbol{k}) R_{\kappa,l}(r, \varepsilon_{i,\boldsymbol{k}}) Y_{lm}(\widehat{\boldsymbol{r}}). \tag{14}$$

As shown in Supplementary Equations (1)–(4), the spherical-band approximation, which separates the radial (k) and angular ($\widehat{\boldsymbol{k}}$) dependencies on the wavevector $\boldsymbol{k}$ as

$$a_{i\kappa,lm}(\boldsymbol{k}) = a_{i\kappa,l}(k) Y^*_{lm}(\widehat{\boldsymbol{k}}), \tag{15}$$

along with the separation of radial (r) and angular ($\widehat{\boldsymbol{r}}$) components of $\boldsymbol{r}$, is crucial. This approximation enables a significant simplification of the MH parameter $\widetilde{\eta}_\kappa$, reducing Eq. (9) to

$$\widetilde{\eta}_\kappa = \sum_l \frac{2(l+1)}{(2l+1)(2l+3)} M^2_{\kappa;l,l+1} \frac{n_{\kappa,l}(r_{\kappa,\text{MT}}, \varepsilon_F) \times n_{\kappa,l+1}(r_{\kappa,\text{MT}}, \varepsilon_F)}{N(\varepsilon_F)}, \tag{16}$$

where the partial EP matrix elements are defined as an integral of two normalized radial functions with the potential gradient over the MT-sphere volume,

$$M_{\kappa;l,l+1}(r_{\kappa,\text{MT}}, \varepsilon_F) = \frac{\int_0^{r_{\kappa,\text{MT}}} dr r^2 R_{\kappa,l}(r,\varepsilon_F) \frac{dV_\kappa(r)}{dr} R_{\kappa,l+1}(r,\varepsilon_F)}{\sqrt{\int_0^{r_{\kappa,\text{MT}}} dr r^2 R^2_{\kappa,l}(r,\varepsilon_F) \int_0^{r_{\kappa,\text{MT}}} dr r^2 R^2_{\kappa,l+1}(r,\varepsilon_F)}}. \tag{17}$$

As a result of the spherical-band approximation, Eq. (16) includes only partial EP matrix elements corresponding to dipole transitions with $\Delta l = \pm 1$. The quantities $n_{\kappa,l}$ represent the partial eDOS for angular momentum l inside the MT sphere of atom κ, defined as

$$\begin{aligned} n_{\kappa,l}(r_{\kappa,\text{MT}}; \varepsilon_F) &= \sum_m n_{\kappa,lm}(r_{\kappa,\text{MT}}; \varepsilon_F) \\ &= \sum_m \frac{\Omega}{(2\pi)^3} \int_0^{r_{\kappa,\text{MT}}} dr r^2 R^2_{\kappa,l}(r, \varepsilon_F) \\ &\quad \times \sum_i \int_{\text{BZ}} d\boldsymbol{k}\delta(\varepsilon_{i,\boldsymbol{k}} - \varepsilon_F) \left|a_{i\kappa,lm}(\boldsymbol{k})\right|^2. \end{aligned} \tag{18}$$

It is important to point out that the spherical-band approximation is not required for the partial eDOS calculation, as can be seen in Eq. (18), where general coefficients $a_{i\kappa,lm}(\boldsymbol{k})$ are used.

Hereafter, the task of computing MH parameters in PP+PW codes comes down to the calculation of partial EP matrix elements and partial eDOS.

Formulation 1: partial EP matrix elements on the MT sphere

The original expression for the partial EP matrix elements, introduced by Gaspari and Gyorffy [Eq. (17)][1,2], involves the integration of the radial functions $R_{\kappa,l}(r, \varepsilon_F)$ and $R_{\kappa,l+1}(r, \varepsilon_F)$, along with the derivative of the MT potential $dV_\kappa(r)/dr$, over the volume of the MT sphere (Fig. 2a). This expression has three problems for the PP + PW codes: (1) The pseudo (PS) potential differs from the all-electron (AE) potential within a cut-off radius r_c, where pseudization takes place (Fig. 2b), rendering the integration of the PS-potential derivative in that region unreliable; (2) The screened self-consistent potential, as calculated in PP + PW codes, is periodic in the real space, and needs to be converted to localized screened atomic potentials; (3) The radial functions $R_{\kappa,l}(r, \varepsilon)$ are not calculated explicitly and need to be derived from available DFT data.

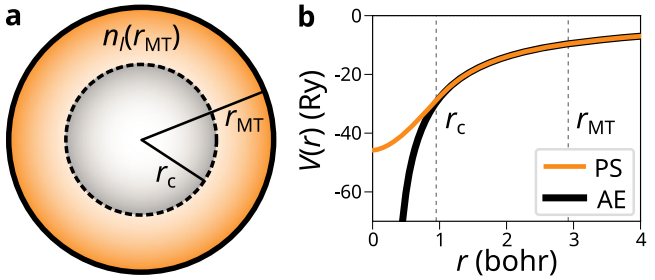

Fig. 2 | Comparison of pseudo and all-electron potentials. a Spatial relationship between the muffin-tin radius r_{MT} and the pseudopotential cut-off radius r_c, showing that r_c is smaller than r_{MT}. **b** Radial profiles of the pseudo (PS) potential and all-electron (AE) potential. The PS potential (orange line) deviates from the AE potential (black line) at radii below r_c.

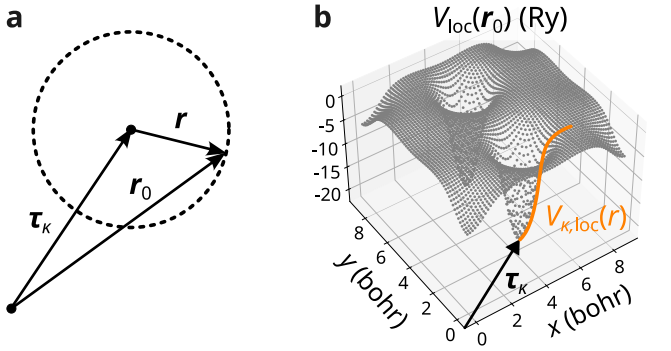

Fig. 3 | Extraction of the local screened atomic potential. a Spatial relationship between the real-space grid $\boldsymbol{r}$ centered on the atom at position $\boldsymbol{\tau}_\kappa$ and the grid $\boldsymbol{r}_0$ centered on the origin of the unit cell. **b** Radial profile of the spherically symmetric atomic local potential $V_{\kappa,\mathrm{loc}}(r)$, isolated from the total periodic potential.

In our method, the first problem is solved by referring to the following reformulated expression for Eq. (17):

$$M_{\kappa;l,l+1}(r_{\mathrm{MT}},\varepsilon_{\mathrm{F}}) = \left.\frac{[V_\kappa(r)-\varepsilon_{\mathrm{F}}]r^2-(L_{\kappa,l}-l)[L_{\kappa,l+1}+(l+2)]}{r\sqrt{\frac{\partial L_{\kappa,l}}{\partial\varepsilon}\cdot\frac{\partial L_{\kappa,l+1}}{\partial\varepsilon}}}\right|_{\substack{\varepsilon=\varepsilon_{\mathrm{F}}\\ r=r_{\kappa,\mathrm{MT}}}},$$
$$L_{\kappa,l}(r,\varepsilon) = \frac{r}{R_{\kappa,l}(r,\varepsilon)}\left(\frac{\partial R_{\kappa,l}(r,\varepsilon)}{\partial r}\right). \quad (19)$$

It was introduced by Pettifor[12] based on the Schrödinger equation for the radial functions $R_{\kappa,l}(r,\varepsilon)$ and their normalization conditions, provided in Supplementary Equation (8). Here, $V_\kappa(r)$ is the local screened potential of the atom κ, $L_{\kappa,l}(r,\varepsilon)$ is the logarithmic derivative of the radial part of the wavefunction evaluated around the Fermi level, and $\partial L_{\kappa,l}/\partial\varepsilon$ is the energy derivative of the logarithmic derivative. In this expression, the values of the potential and logarithmic derivatives at the MT radius are sufficient to calculate the partial EP matrix elements.

The second problem is addressed by exploiting properties of the Fourier transform. The self-consistent DFT-screened PS potential is given as a periodic local screened potential $V_{\mathrm{loc}}(\boldsymbol{r}_0)$ (Fig. 3b), defined on the 3D real-space grid $\boldsymbol{r}_0$ and centered at an arbitrary origin of the calculated unit cell. Its Fourier transform is represented by the coefficients

$$\widetilde{V}(\boldsymbol{G}) = \frac{1}{\Omega}\int_{\Omega} d\boldsymbol{r}_0 e^{-i\boldsymbol{G}\cdot\boldsymbol{r}_0} V_{\mathrm{loc}}(\boldsymbol{r}_0), \quad (20)$$

where $\boldsymbol{G}$ is a reciprocal lattice vector.

A spherically-symmetric local screened atomic potential, $V_{\kappa,\mathrm{loc}}(r)$, is then obtained in Eq. (21) by extracting the coefficients of the plane-wave expansion of the periodic potential on a shifted grid, $\boldsymbol{r}$, centered on a specific atom at $\boldsymbol{\tau}_\kappa$ (Fig. 3a, b), and by retaining only the $l = m = 0$ term in the expansion of $e^{i\boldsymbol{G}\cdot\boldsymbol{r}}$ in spherical Bessel functions and spherical harmonics (see Supplementary Equation (9) for details).

$$V_{\kappa,\mathrm{loc}}(r) = V_{\kappa,\mathrm{loc}}(|\boldsymbol{r}_0 - \tau_\kappa|) = \sum_{\boldsymbol{G}} e^{i\boldsymbol{G}\cdot\tau_\kappa}\widetilde{V}(\boldsymbol{G})\frac{\sin Gr}{Gr}. \quad (21)$$

In this equation, $e^{i\boldsymbol{G}\cdot\tau_\kappa}\widetilde{V}(\boldsymbol{G})$ are modified coefficients of the plane-wave expansion of the same periodic potential $V_{\mathrm{loc}}(\boldsymbol{r})$ [Fig. 3b], which is now evaluated on the grid $\boldsymbol{r}$. Since $V_{\mathrm{loc}}(\boldsymbol{r})$ is DFT-screened, the extracted local PS potential $V_{\kappa,\mathrm{loc}}(r)$ is also screened. Note that the local PS coincides with the AE potential above the cut-off radius: $V_\kappa(r) = V_{\kappa,\mathrm{loc}}(r)\ \forall\ r > r_c$.

For the third problem, the method of choice is to generate the radial functions $R_{\kappa,l}(r,\varepsilon)$, which are compatible with the extracted screened potential $V_{\kappa,\mathrm{loc}}(r)$, for a particular energy ε by solving the corresponding

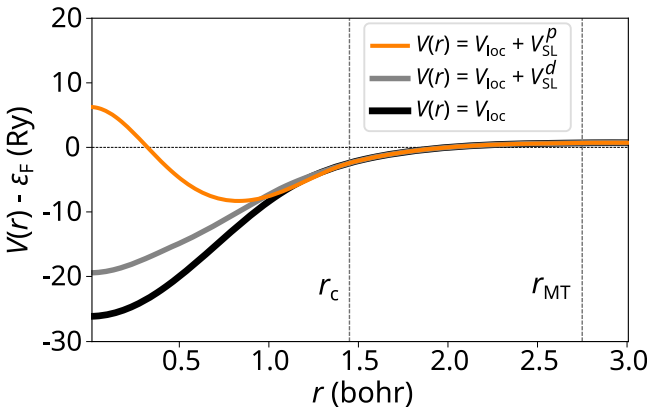

Fig. 4 | Contributions of semilocal *l*-dependent components to the local pseudopotential in bcc-Nb. The purely local potential (black line) is compared to the total potential (solid gray and orange lines) after the inclusion of angular-momentum-dependent semilocal terms.

radial Schrödinger equation,

$$\left[-\frac{d^2}{dr^2} + V^l_{\kappa,\mathrm{eff}}(r)\right]\left[rR_{\kappa,l}(r,\varepsilon)\right] = \varepsilon\left[rR_{\kappa,l}(r,\varepsilon)\right]\big|_{\varepsilon=\varepsilon_{\mathrm{F}}}, \quad (22)$$

with the effective potential $V^l_{\kappa,\mathrm{eff}}(r)$ containing $V_{\kappa,\mathrm{loc}}(r)$, the l-dependent semilocal (SL) potential $V^l_{\kappa,\mathrm{SL}}(r)$ that is non-zero only in the core region $r < r_c$ (see Fig. 4), and the centrifugal potential $l(l+1)/r^2$:

$$\begin{aligned} V^l_{\kappa,\mathrm{eff}}(r) &= V_\kappa(r) + \tfrac{l(l+1)}{r^2} \\ &= \left[V_{\kappa,\mathrm{loc}}(r) + V^l_{\kappa,\mathrm{SL}}(r)\right] + \tfrac{l(l+1)}{r^2}. \end{aligned} \quad (23)$$

Equation (22) is solved numerically at the specified energy ε by outward integration from an r value close to zero to the desired MT radius. This way, the derivatives $\partial L_{\kappa,l}/\partial\varepsilon$ can be obtained by solving the radial Schrödinger equation at different energies close to the Fermi level. The contribution from the SL potential is pertinent to the PS approach: Different pseudopotentials are needed to generate radial functions for different l values, while only one AE potential would generate all radial functions.

Although most PP+PW codes use pseudopotentials in the non-local (NL) Vanderbilt-Kleinman-Bylander (VKB) form[74–76], which depends on both r and r', we adopt the SL form in the current implementation for simplicity. Here, we employ the non-local optimized norm-conserving Vanderbilt pseudopotentials (ONCVPSP) developed by Hamann[77,78]. The

automatic conversion of the NL components read directly from the pseudopotential file to the SL form is straightforward and described in Supplementary Equations (10)–(12). In principle, solving the radial Schrödinger equation with NL potentials directly[79] would yield the same results.

Formulation 2: partial eDOS inside the MT sphere

The partial eDOS inside the MT sphere of atom κ is derived by assuming that on the surface of the MT sphere the wavefunction of state i can be expanded simultaneously in spherical harmonics and plane waves:

$$\begin{cases} \Psi_{i,\boldsymbol{k}}(\boldsymbol{r}) = \sum_{lm} a_{i\kappa,lm}(\boldsymbol{k}) R_{\kappa,l}(r_{\kappa,\mathrm{MT}}, \varepsilon_{i,\boldsymbol{k}}) Y_{lm}(\widehat{\boldsymbol{r}}), \\ \Psi_{i,\boldsymbol{k}}(\boldsymbol{r}) = \psi_{i,\boldsymbol{k}}(\boldsymbol{\tau}_\kappa + \boldsymbol{r})\Big|_{r=r_{\kappa,\mathrm{MT}}} = \frac{1}{\sqrt{\Omega}} \sum_{\boldsymbol{G}} e^{i(\boldsymbol{k}+\boldsymbol{G})\cdot(\boldsymbol{\tau}_\kappa+\boldsymbol{r})} \widetilde{\psi}_i(\boldsymbol{k}+\boldsymbol{G})\Big|_{r=r_{\kappa,\mathrm{MT}}}, \end{cases} \tag{24}$$

where $\widetilde{\psi}_i(\boldsymbol{k}+\boldsymbol{G})$ are coefficients of the Fourier expansion of the wavefunction $\Psi_{i,\boldsymbol{k}}(\boldsymbol{r})$.

From the system of Eq. (24), the coefficients $a_{i\kappa,lm}(\boldsymbol{k})$ are determined from Eq. (25), evaluated using the Gauss-Legendre quadrature method[80].

$$a_{i\kappa,lm}(\boldsymbol{k}) = \frac{1}{\sqrt{\Omega} R_{\kappa,l}(r,\varepsilon_{i,\boldsymbol{k}})} \int d\widehat{\boldsymbol{r}} \left[\sum_{\boldsymbol{G}} e^{i(\boldsymbol{k}+\boldsymbol{G})\cdot(\boldsymbol{\tau}_\kappa+\boldsymbol{r})} \widetilde{\psi}_i(\boldsymbol{k}+\boldsymbol{G}) \right] Y^*_{lm}(\widehat{\boldsymbol{r}})\Big|_{r=r_{\kappa,\mathrm{MT}}}. \tag{25}$$

Then, using Eq. (25) and Supplementary Equation (4), the partial eDOS, $n_{\kappa,l}$, can be obtained from the Fourier coefficients, $\widetilde{\psi}_i(\boldsymbol{k}+\boldsymbol{G})$, and the logarithmic derivatives, $\partial L_{\kappa,l}/\partial\varepsilon$, by Eq. (26). Note that this method allows for the calculation of not only the l-resolved eDOS, but also m-resolved eDOS, $n_{\kappa,lm}$.

$$\begin{aligned} n_{\kappa,l}(r_{\kappa,\mathrm{MT}}, \varepsilon_\mathrm{F}) &= \sum_{m=-l}^{l} n_{\kappa,lm}(r_{\kappa,\mathrm{MT}}, \varepsilon_\mathrm{F}) \\ &= \sum_{m=-l}^{l} \frac{r_{\kappa,\mathrm{MT}}}{(2\pi)^3} \left(-\frac{\partial}{\partial\varepsilon} L_{\kappa,l}\right) \int_{\mathrm{BZ}} d\boldsymbol{k} \sum_{i=1}^{N_\mathrm{states}} \delta(\varepsilon_{i,\boldsymbol{k}} - \varepsilon_\mathrm{F}) \\ &\quad \times \left| \int d\widehat{\boldsymbol{r}} \left[\sum_{\boldsymbol{G}} e^{i(\boldsymbol{k}+\boldsymbol{G})\cdot(\boldsymbol{\tau}_\kappa+\boldsymbol{r})} \widetilde{\psi}_i(\boldsymbol{k}+\boldsymbol{G}) \right] Y^*_{lm}(\widehat{\boldsymbol{r}}) \right|^2 \Big|_{\substack{r = r_{\kappa,\mathrm{MT}} \\ \varepsilon = \varepsilon_\mathrm{F}}}. \end{aligned} \tag{26}$$

As can be seen from Eq. (19), the squared partial EP matrix element, $M^2_{l,l+1}$, contains the energy derivatives $\partial L_{\kappa,l}/\partial\varepsilon$ and $\partial L_{\kappa,l+1}/\partial\varepsilon$ in the denominator. These derivatives are normalization integrals for the radial functions R_l and R_{l+1} (see Supplementary Equation (8)) that cancel out when $M^2_{l,l+1}$ is multiplied by the partial eDOS n_l and n_{l+1} from Eq. (26). Hence, if the calculation of the partial eDOS themselves is not required, Eq. (16) for the MH parameters can be rewritten in a form independent of $\partial L_{\kappa,l}/\partial\varepsilon$ and $\partial L_{\kappa,l+1}/\partial\varepsilon$, therefore the normalization integrals do not have to be computed.

The eDOS at the Fermi level per cell per spin is calculated as a Brillouin-zone integral of the delta-functions summed over all electronic states,

$$N(\varepsilon_\mathrm{F}) = \frac{\Omega}{(2\pi)^3} \int_{\mathrm{BZ}} d\boldsymbol{k} \sum_i \delta(\varepsilon_{i,\boldsymbol{k}} - \varepsilon_\mathrm{F}). \tag{27}$$

Formulation 3: evaluation of the ionic factor

Evaluation of the on-site blocks $\Phi_{\kappa\kappa}$ defined in Eqs. (6) and (7) instead of the full IFC matrix eliminates the need for large supercells and dense $\boldsymbol{k}$-grids required to capture the long-range nature and often oscillatory behavior of its off-site elements in metals. In practice, converged ionic factors can be obtained from SCF forces using standard displacements of non-equivalent atoms along symmetry-distinct directions in relatively small (super)cells of about 8 to 64 atoms [see Supplementary Equations (13)–(17) and Table S3 for details][81]. However, this approach can become computationally expensive for low-symmetry structures with multiple atomic types.

To provide an efficient alternative transferable across materials classes, this work also leverages a modern uMLP to approximate the full IFC matrix at a fraction of the DFT cost. Our tests illustrate that extracted local $\widetilde{\phi}_\kappa$ values are in excellent agreement with finite-displacement DFT results.

Formulation 4: estimates of the critical temperature

Estimates of the critical temperature using the empirical McMillan formula[61,82],

$$T_\mathrm{c} = \frac{\omega_\mathrm{ln}}{1.2} \exp\left[-\frac{1.04(1+\lambda)}{\lambda - \mu^*(1+0.62\lambda)} \right], \tag{28}$$

require the logarithmic-average phonon frequency, ω_ln, that is defined[83,84] as the limit of the moments $\langle\omega^n\rangle^{1/n}$:

$$\langle\omega^n\rangle = \frac{\int d\omega \omega^{n-1}\alpha^2F(\omega)}{\int d\omega\omega^{-1}\alpha^2F(\omega)} = \frac{2}{\lambda}\int d\omega\omega^{n-1}\alpha^2F(\omega), \tag{29}$$

$$\omega_\mathrm{ln} = \lim_{n\to 0} \langle\omega^n\rangle^{1/n} = \exp\left[\frac{2}{\lambda} \int d\omega\omega^{-1}\alpha^2F(\omega)\ln\omega \right]. \tag{30}$$

Here, μ^* is the Coulomb pseudopotential and $\alpha^2F(\omega)$ is the Eliashberg spectral function. Since the RMTA does not provide $\alpha^2F(\omega)$, ω_ln is typically[4,22,36,81,84] approximated via the second-moment average, $\langle\omega^2\rangle$[4,61,84],

$$\omega_\mathrm{ln} \approx \sqrt{\langle\omega^2\rangle}. \tag{31}$$

If the phonon spectrum is represented by a set of discrete modes, $\omega_\nu \equiv \omega_\kappa|_{\forall\kappa\in\{\nu\}}$, with individual coupling constants, then Eq. (30) is strictly equivalent[32,85] to

$$\omega_\mathrm{ln} = \prod_\nu^{N_\mathrm{types}} \omega_\nu^{\lambda_\nu/\lambda} = \prod_\kappa^{N_\mathrm{atoms}} \widetilde{\omega}_\kappa^{\lambda_\kappa/\lambda}. \tag{32}$$

In this case, the characteristic phonon frequencies, ω_κ, can be approximated from Eq. (8) as

$$\omega_\kappa = \sqrt{\langle\omega^2_\kappa\rangle} \approx \frac{1}{\sqrt{M_\kappa\widetilde{\phi}_\kappa}}. \tag{33}$$

In Eq. (28), the Coulomb pseudopotential μ^* is defined as $\mu/[1+\mu\ln(W/\Omega)]$[34,86–88], where μ is the unrenormalized Coulomb potential, a quantity of the order of one, and $W/\Omega \gg 1$ is the ratio of the electronic and ionic energy scales. To a good approximation, $\mu^* \approx 1/\ln(W/\Omega) \approx 0.13$ for most metals[61]. Unless otherwise stated, this μ^* value is used to estimate T_c in the present work.

Quantitative verification

A key difference in how the partial EP matrix elements and MH parameters depend on the choice of the MT radius is illustrated in Fig. 5a, b for the bcc structure of Nb. For all l channels, $M^2_{l,l+1}$ decrease as the MT radius increases [Fig. 5a], consistent with Pettifor's observation[12] that partial EP matrix elements alone are not sufficient to describe the electronic part of the EPC constant because they are strongly dependent on the MT radius.

On the contrary, the partial MH parameters, which are presented in eV/Å^2 following previous studies[12,14,16], appear to be less sensitive [Fig. 5b] to the choice of the MT radius since they include the partial eDOS, which increases as the MT sphere expands. Notably, while the *df* channel may seem dominant based on its corresponding partial EP matrix element, it

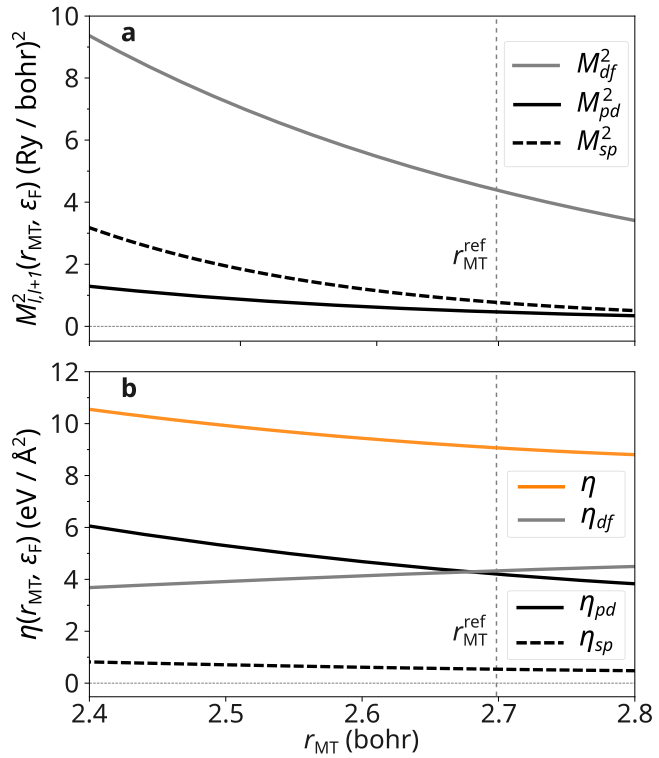

Fig. 5 | Muffin-tin radius dependence of partial electron-phonon matrix elements and McMillan-Hopfield parameters. a Partial electron-phonon matrix elements ($M^2_{l,l+1}$) for a Nb atom in the bcc structure. **b** Partial ($\eta_{l,l+1}$) and total (η) McMillan-Hopfield parameters. All quantities are shown as functions of the muffin-tin (MT) radius (r_{MT}). The reference MT radius ($r^{ref}_{MT} = 2.70$ bohr) is indicated by vertical dashed lines.

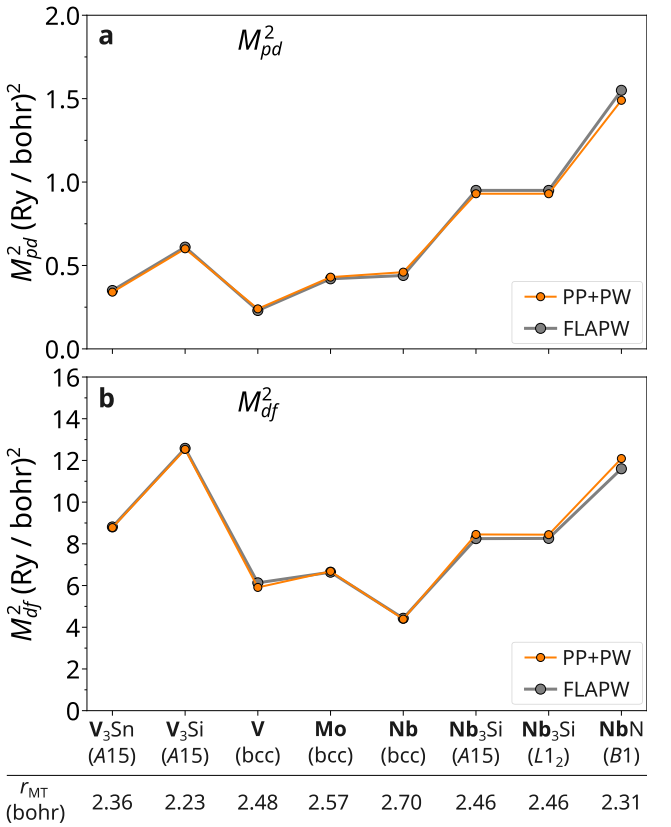

Fig. 6 | Comparison of squared partial electron-phonon matrix elements between pseudopotential and all-electron methods. a Squared partial electron-phonon matrix elements ($M^2_{l,l+1}$) for the *pd* channel ($l = 1$) calculated for V, Mo, and Nb atoms across various crystallographic structures. **b** Matrix elements for the *df* channel ($l = 2$) for the same set of atoms and structures. Results obtained via the pseudopotential-based plane-wave (PP + PW) method (orange circles) are compared against full-potential linearized augmented plane-wave (FLAPW) calculations (gray circles). Corresponding muffin-tin (MT) radii for each metal species are indicated at the bottom of the figure.

contributes roughly the same to the total MH parameter η as the *pd* channel at the reference MT radius. Achieving a nearly flat behavior of the total atomic MH parameter around the reference MT radius was one of the objectives of this work. Nevertheless, the slight dependence on r_{MT} indicates that careful selection of the MT radius based on the cell geometry is advisable.

The good agreement between the PP+PW and FLAPW methods for the electronic factor calculated in selected simple metals and compounds is demonstrated in Figs. 6 and 7, where the *Strukturbericht* symbols[89] are used as space-group identifiers for the compounds. Crystallographic parameters of the structures are provided in Table S1. The differences in the squared partial EP matrix elements (*pd* and *df*) for the metal atoms in the selected structures do not exceed 5% [Fig. 6], with the PP+PW and FLAPW results almost overlapping. In Fig. 7, which shows the MH parameters for the symmetry types of the metal atoms, both the partial and total MH parameters exhibit similar trends across the two methods. Both methods demonstrate that the η parameter of Nb atoms in NbN is mostly dominated by the *df* channel contribution, in agreement with previous studies[16,21]. The observed discrepancies between PP + PW and FLAPW are primarily due to slight differences in the electronic density of states. Importantly, there is no tendency for one of the methods to produce consistently higher values than the other. Comparison of the total MH parameters, shown as circles in Fig. 7, to some previous APW results[14,16] is provided in Fig. S2.

The MH parameters, combined with the recipes for evaluating the local lattice response outlined above, are then used to obtain the total EPC constant and estimate the critical temperature. Table 1 summarizes the MH parameters, ionic factors, and both type-resolved and total EPC constants for the four considered materials—three simple metals and one *A*15 compound. The ϕ_ν values from Phonopy + VASP finite-displacement supercell calculations with pseudopotentials (denoted as DFT) reproduce the DFPT results well, showing maximum differences of 11% in bcc-V and 16% in fcc-Pd. The corresponding results obtained using Phonopy+eSEN (denoted as uMLP) match the underlying DFT reference with similar accuracy, as the deviations range between 1% in bcc-Nb and 11% in bcc-V.

The resulting EPC constants, evaluated with either DFT- or uMLP-based ionic factors, also align with the DFPT values within a 16% margin. This level of agreement is comparable to the ~20% spread between the present and previously reported DFPT EPC values for these materials[90–94], arising in part from slight variations in lattice parameters, Brillouin-zone sampling, and smearing choices in the DFPT calculations[95].

Table 2 lists the logarithmic-average frequencies and critical temperatures, T_c, evaluated with $\mu^* = 0.13$, along with the μ^* values used in the reference DFPT studies. In bcc-Nb and bcc-V, the experimental T_c is commonly reproduced by shifting the dynamic pair-breaking effect of spin fluctuations, which effectively reduces the total EPC by $\lambda_{spin} = 0.21 - 0.34$ [96–98], into the static electron-electron repulsion, which artificially inflates μ^* up to 0.30[90,92]. The ω_{ln} values show that approximating the logarithmic-average frequency with the second-moment average in the RMTA systematically overestimates this quantity by 2 to 12%. This trend agrees with previous reports of phonon-frequency moments[84,91], where higher-order moments yield larger ω_{ln} estimates. Consequently, the RMTA produces systematically higher T_c values even when μ^* is chosen consistently, indicating that the EPC constants obtained with the RMTA are more reliable than the corresponding T_c estimates.

Analysis of Tables 1 and 2 shows that the highest and lowest calculated η_ν correspond to the highest and lowest DFPT T_c references, respectively.

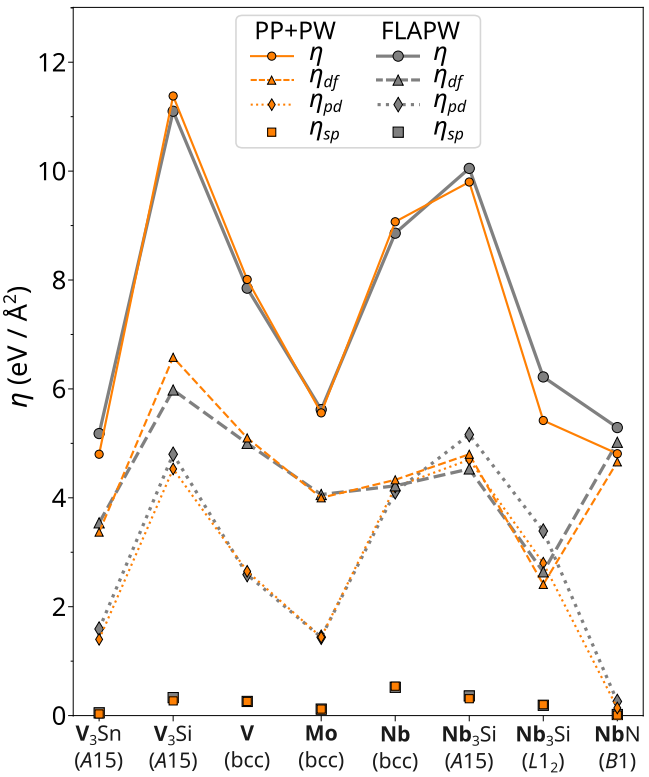

Fig. 7 | Comparison of type-resolved McMillan–Hopfield parameters between pseudopotential and all-electron methods. Partial ($\eta_{l,l+1}$) and total (η) parameters calculated for V, Mo, and Nb atoms across various crystallographic structures. Results obtained using the pseudopotential-based plane-wave (PP+PW) method (orange circles) are compared with full-potential linearized augmented plane-wave (FLAPW) calculations (gray circles).

The low calculated electronic factor, EPC constant, and T_c values in fcc-Pd correctly indicate that it is not a conventional superconductor[91].

Discussion

The method presented for implementing the rigid muffin-tin approximation in PP+PW codes enables the calculation of the electronic factor of the EPC constant, expressed through the MH parameter. The values obtained for a variety of simple metals and compounds are validated against results from an FLAPW code. The excellent agreement in the partial EP matrix elements and MH parameters between the PS- and AE-potential methods confirms the reliability of the implementation.

To obtain full EPC constants and critical temperatures, the electronic factor is combined with an ionic factor derived from the averaged diagonal elements of the on-site IFC matrix block. This block can be efficiently evaluated using ab initio or uMLP-based finite displacements. The resulting RMTA EPC constants for the considered materials show good agreement with the DFPT references. These results suggest that the combined electronic and ionic RMTA workflow can reliably distinguish between materials with low and high EPC constants.

Computing the electronic factor has a cost comparable to that of an SCF run in Quantum ESPRESSO (QE) package[99,100,101], while the evaluation of the ionic factor is significantly accelerated by using uMLPs in finite-displacement calculations with Phonopy. In our tests, the uMLP calculations were at least three orders of magnitude faster than their DFT equivalents, yielding converged ionic factors within a typical runtime of the ab initio electronic factor evaluation. Although further development is required to integrate these components into a single workflow and software package, the approach presented here already enables efficient estimation of EPC constants and critical temperatures for a broad range of transition-metal compounds.

Machine learning studies[26,27,102] have demonstrated that MH parameters and partial eDOS can serve as effective descriptors for identifying potential superconductors. In this context, the RMTA-derived MH para-

Table 1 | Electron-phonon coupling constants calculated within the rigid muffin-tin approximation

Phase	Type	$r_{\kappa,MT}$	η_ν	ϕ_ν			λ_ν		λ			
	ν		DFT	DFT	uMLP	DFPT	DFT	uMLP	DFT	uMLP	DFPT	Refs.
bcc-V	V	2.48	8.01	0.158	0.176	0.177	1.27	1.41	1.27	1.41	1.47	1.19–1.22[a,c]
bcc-Nb	Nb	2.70	9.07	0.137	0.135	0.132	1.24	1.22	1.24	1.22	1.36	1.22–1.26[a,c]
fcc-Pd	Pd	2.66	2.65	0.121	0.125	0.144	0.32	0.33	0.32	0.33	0.29	0.35–0.38[a,b]
A15-V_3Si	V	2.23	11.37	0.136	0.143	0.145	1.55	1.63	1.56	1.64	1.41	1.15–1.26[d,e]
	Si	2.76	0.17	0.100	0.106	0.107	0.02	0.02				

Total electron-phonon coupling (EPC) constant, λ, is obtained based on QE-implemented DFT type-resolved McMillan-Hopfield parameters, η_ν (eV/Å^2), at the specified MT radii, $r_{\kappa,MT}$ (bohr), and ionic factors, ϕ_ν (Å^2/eV), from Phonopy+VASP DFT and Phonopy+eSEN uMLP finite-displacement calculations for selected materials. All finite-displacement calculations employed 216-atom cells. DFPT λ values obtained in this work (DFPT) and corresponding references (Refs.) are provided for comparison. $\kappa \in \{\nu\}$ is assumed.
a[90], b[91], c[92], d[93], e[94].

Table 2 | Logarithmic-average frequencies and superconducting critical temperatures

Phase	ω_{ln}				$T_c(\mu^* = 0.13)$			$T_c(\mu^*)\,\forall\,\mu^* \in [\mu^*_{max}, \mu^*_{min}]$				$[\mu^*_{max}, \mu^*_{min}]$
	DFT	uMLP	DFPT	Refs.	DFT	uMLP	DFPT	DFT	uMLP	DFPT	Refs.	Refs.
bcc-V	265	251	187	202–245[a,c]	23	24	19	9	11	9	6–7[a,c]	[0.30][a,c]
bcc-Nb	211	212	139	124–185[a,c]	18	17	13	12–16	12–16	9–12	9–11[a,c]	[0.21, 0.15][a,c]
fcc-Pd	209	206	135	174–180[a,b]	<1	<1	<1	<1	<1	<1	<1[b]	[0.15, 0.10][b]
A15-V_3Si	286	279	202	255–259[d,e]	31	33	20	29–34	30–35	18–22	17–26[d,e]	[0.15, 0.10][d,e]

Calculated logarithmic-average frequency, ω_{ln} (K), and critical temperature, T_c (K), are based on the type-resolved McMillan-Hopfield parameters, η_ν, and ionic factors, ϕ_ν, from Table 1. DFPT ω_{ln}, μ^*_{max}, μ^*_{min}, $T_c(\mu^*)\,\forall\,\mu^* \in [\mu^*_{max}, \mu^*_{min}]$ calculated in this work (DFPT) and corresponding references (Refs.) are provided for comparison.
a[90], b[91], c[92], d[93], e[94].

meters and full EPC constants are well-suited for high-throughput screening of candidate materials. While T_c estimates can also be used, their systematic overestimation arising from the approximation of the logarithmic-average phonon frequency must be considered. To improve the RMTA predictions for *sp*-metals and other families of materials, corrections to the asymptotic behavior of the local ionic potential could be introduced, as was done by Zdetsis et al.[38] and Mazin et al.[19].

Methods

Calculation of the electronic factors

The present implementation for evaluating the electronic factor was developed within the Quantum ESPRESSO package[99–101], which was employed in this study to calculate the self-consistent screened PS potentials with the PW code. Norm-conserving ONCVPSP[77,78] pseudopotentials with the Perdew-Burke-Ernzerhof (PBE)[103] generalized-gradient approximation (GGA) for the exchange-correlation functional were used for all atoms, with a wavefunction energy cutoff of 120 Ry. The RMTA code was executed as a postprocessing step after the SCF calculation. In the "Quantitative verification" section, all structures were modeled with their primitive unit cells, and the MT radii were chosen to correspond to touching spheres. These values were estimated from the nearest-neighbor distances divided into ratios of the corresponding default MT radii commonly used in (FL)APW calculations[16]. The default three-dimensional fast Fourier transform (FFT) mesh for charge density and self-consistent potential, set by the energy cutoff, was retained. A $24 \times 24 \times 24$ automatic Monkhorst-Pack $\boldsymbol{k}$-point grid and Methfessel-Paxton smearing[104] with $\sigma = 10^{-2}$ Ry were utilized for the approximation of the occupation function in the SCF calculation. The tetrahedron integration method[105] on the same $\boldsymbol{k}$-point grid was selected for the evaluation of the partial and total eDOS across all structures, since it showed faster convergence with respect to the $\boldsymbol{k}$-point grid than smeared delta-function approximations (see Fig. S1a, b).

Calculated partial EP matrix elements and McMillan-Hopfield parameters were compared to the FLAPW code *flair*[106]. In FLAPW, semicore states of all atoms were treated as core with explicit core-orthogonalization. Equations (16) and (19) were evaluated with the atomic potential, radial functions, and partial and total eDOS calculated using the FLAPW method. The same MT radii, $\boldsymbol{k}$-point grid, and smearing parameters as those used for the RMTA calculations with the PW code were employed to ensure consistency.

Calculation of the ionic factors

The ionic factors were computed via the finite-displacement method in supercells using Phonopy[107,108] interfaced with the Vienna ab initio simulation package (VASP)[109–113] and eSEN[65]. To keep both the MH parameters and ionic factors local, only the on-site 3×3 atomic blocks of the resulting IFC matrices were extracted and used following the methodology described in the "Assumption 2: local-vibration approximation" section. The ϕ_ν uMLP values were found to be within ~10% of the DFT Phonopy+VASP results obtained with the projector augmented wave (PAW) PBE pseudopotentials (see Fig. S3a–h and Table S2 for convergence tests). Phonopy was used to set up and post-process calculations with 0.1 Å displacements in large supercells containing 216 atoms to ensure good convergence in the considered materials, especially in bcc-Nb[114]. The supercell DFT reference calculations performed with VASP employed a 500 eV energy cutoff and Monkhorst-Pack $\boldsymbol{k}$-point grid of $4 \times 4 \times 4$.

Reference DFPT calculations

Reference DFPT calculations of ϕ_ν, λ, and $\omega_{\ln}$ were performed with QE, employing the same pseudopotentials and wavefunction energy cutoffs as those chosen for the electronic factor calculations. A $24 \times 24 \times 24$ $\boldsymbol{k}$-grid and an $8 \times 8 \times 8$ $\boldsymbol{q}$-grid were set for the primitive cells of the simple metals, while a $12 \times 12 \times 12$ $\boldsymbol{k}$-grid and a $4 \times 4 \times 4$ $\boldsymbol{q}$-grid were adopted for the *A*15 compound. In the $\alpha^2F(\omega)$ calculation, a Gaussian smearing of 0.121 THz was applied to the phonon delta-function, and a Gaussian smearing of 0.02 Ry was selected for the electronic delta-function. The convergence tests with respect to the size of the $\boldsymbol{q}$-grid are provided in Fig. S4a–d.

Data availability

The data supporting this work are available within the paper, its Supplementary Information files, and from the corresponding author upon reasonable request.

Code availability

The RMTA code for Quantum ESPRESSO is available from the corresponding author upon reasonable request. Quantum ESPRESSO, *flair*, VASP, and Phonopy codes used in this study are distributed via their corresponding websites.

Received: 28 August 2025; Accepted: 8 May 2026;
Published online: 23 May 2026

References

1. Gaspari, G. D. & Gyorffy, B. L. Electron-phonon interactions, *d* resonances, and superconductivity in transition metals. *Phys. Rev. Lett.* **28**, 801–805 (1972).
2. Evans, R., Gaspari, G. D. & Gyorffy, B. L. A simple theory of the electron-phonon mass enhancement in transition metals. *J. Phys. F Met. Phys.* **3**, 39 (1973).
3. Gomersall, I. R. & Gyorffy, B. L. A simple theory of the electron-phonon mass enhancement in transition metal compounds. *J. Phys. F Met. Phys.* **4**, 1204 (1974).
4. Klein, B. M. & Papaconstantopoulos, D. A. Electron-phonon interaction and superconductivity in transition metals and transition-metal carbides. *Phys. Rev. Lett.* **32**, 1193–1195 (1974).
5. Slater, J. C. Wave functions in a periodic potential. *Phys. Rev.* **51**, 846–851 (1937).
6. Martin, R. M. *Electronic Structure: Basic Theory and Practical Methods* (Cambridge University Press, 2004).
7. Dewhurst, J. K. et al. The ELK code. https://elk.sourceforge.net.
8. Gulans, A. et al. Exciting: A full-potential all-electron package implementing density-functional theory and many-body perturbation theory. *J. Phys. Condens. Matter* **26**, 363202 (2014).
9. Korringa, J. On the calculation of the energy of a Bloch wave in a metal. *Physica* **13**, 392–400 (1947).
10. Kohn, W. & Rostoker, N. Solution of the Schrödinger equation in periodic lattices with an application to metallic lithium. *Phys. Rev.* **94**, 1111–1120 (1954).
11. Butler, W. H., Pinski, F. J. & Allen, P. B. Phonon linewidths and electron-phonon interaction in Nb. *Phys. Rev. B.* **19**, 3708–3721 (1979).
12. Pettifor, D. G. Theory of energy bands and related properties of 4d-transition metals. II. The electron-phonon matrix element, superconductivity and ion core enhancement. *J. Phys. F Met. Phys.* **7**, 1009 (1977).
13. Andersen, O. K. Linear methods in band theory. *Phys. Rev. B.* **12**, 3060–3083 (1975).
14. Papaconstantopoulos, D. A. et al. Calculations of the superconducting properties of 32 metals with $Z \leq 49$. *Phys. Rev. B.* **15**, 4221–4226 (1977).
15. Butler, W. H. Electron-phonon coupling in the transition metals: Electronic aspects. *Phys. Rev. B.* **15**, 5267–5282 (1977).
16. Pickett, W. E. Transferability and the electron-phonon interaction: A reinterpretation of the rigid-muffin-tin approximation. *Phys. Rev. B.* **25**, 745–754 (1982).
17. Ginzburg, V. L. & Kirzhnits, D. A. (eds) *High-temperature superconductivity*, 1982 edn (Kluwer Academic/Plenum, 1982).
18. Mazin, I. I., Savitskii, E. M. & Uspenskii, Y. A. A simple approach to calculation of the phonon-limited electrical resistivity in metals. *Phys. Status Solidi (b)* **112**, 29–33 (1982).

19. Mazin, I. I., Savitskii, E. M. & Uspenskii, Y. A. Electron-phonon effects in 4*d* metals: Calculation of coupling constant and resistivity. *J. Phys. F: Met. Phys.* **14**, 167 (1984).
20. Bose, S. K., Kudrnovsky, J., Mazin, I. I. & Andersen, O. K. Effect of disorder on the electronic structure of palladium. *Phys. Rev. B*. **41**, 7988–7998 (1990).
21. Klein, B. M., Boyer, L. L. & Papaconstantopoulos, D. A. Superconducting properties of *A*15 compounds derived from band-structure results. *Phys. Rev. Lett.* **42**, 530–533 (1979).
22. Raychaudhury, M., Chatterjee, P. & Chatterjee, S. Electron-phonon coupling constant and critical temperature of some *A*15 superconducting compounds of Nb and V. *Phys. Status Solidi (b)* **90**, 609–613 (1978).
23. Jarlborg, T. & Freeman, A. J. Magnetism and superconductivity in *C*15 compounds from self-consistent band calculations. *Phys. Rev. B*. **22**, 2332–2342 (1980).
24. Papaconstantopoulos, D. A. & Klein, B. M. Superconductivity in the palladium-hydrogen system. *Phys. Rev. Lett.* **35**, 110–113 (1975).
25. Papaconstantopoulos, D. A., Mehl, M. J. & Chang, P.-H. High-temperature superconductivity in LaH_{10}. *Phys. Rev. B*. **101**, 060506 (2020).
26. Hutcheon, M. J., Shipley, A. M. & Needs, R. J. Predicting novel superconducting hydrides using machine learning approaches. *Phys. Rev. B*. **101**, 144505 (2020).
27. Shipley, A. M., Hutcheon, M. J., Needs, R. J. & Pickard, C. J. High-throughput discovery of high-temperature conventional superconductors. *Phys. Rev. B*. **104**, 054501 (2021).
28. Gomersall, I. R. & Gyorffy, B. L. Variation of T_c with electron-per-atom ratio in superconducting transition metals and their alloys. *Phys. Rev. Lett.* **33**, 1286–1290 (1974).
29. Pickett, W., Klein, B. & Papaconstantopoulos, D. Theoretical prediction of MoN as a high T_c superconductor. *Phys. B+C* **107**, 667–668 (1981).
30. Mazin, I. & Rashkeev, S. Effect of low symmetry on electron-phonon coupling in perovskite superconductors. *Solid State Commun.* **68**, 93–95 (1988).
31. Mazin, I. & Rashkeev, S. Influence of local symmetry on the electron-phonon coupling in perovskites. *Phys. C Supercond. Appl.* **162-164**, 1347–1348 (1989).
32. Mazin, I. I. et al. Quantitative theory of superconductivity in doped C_{60}. *Phys. Rev. B*. **45**, 5114–5117 (1992).
33. Mazin, I. I. & Dolgov, O. V. Estimation of the electron-phonon coupling in $YBa_2Cu_3O_7$ from the resistivity. *Phys. Rev. B*. **45**, 2509–2511 (1992).
34. Mazin, I. & Antropov, V. Electronic structure, electron-phonon coupling, and multiband effects in MgB_2. *Phys. C Supercond.* **385**, 49–65 (2003).
35. Jasiewicz, K. et al. Pressure effects on the electronic structure and superconductivity of $(TaNb)_{0.67}(HfZrTi)_{0.33}$ high entropy alloy. *Phys. Rev. B*. **100**, 184503 (2019).
36. Wiendlocha, B., Tobola, J. & Kaprzyk, S. Search for Sc_3XB(X = In, Tl, Ga, Al) perovskites superconductors and proximity of weak ferromagnetism. *Phys. Rev. B*. **73**, 134522 (2006).
37. Kuderowicz, G. & Wiendlocha, B. The effect of Ni doping on the electronic structure and superconductivity in the noncentrosymmetric $ThCoC_2$. *J. Magn. Magn. Mater.* **546**, 168688 (2022).
38. Zdetsis, A. D., Economou, E. N. & Papaconstantopoulos, D. A. Non-rigid-muffin-tin calculations of the electron-phonon interaction in simple metals. *Phys. Rev. B*. **24**, 3115–3121 (1981).
39. Giannozzi, P., de Gironcoli, S., Pavone, P. & Baroni, S. Ab initio calculation of phonon dispersions in semiconductors. *Phys. Rev. B*. **43**, 7231–7242 (1991).
40. Gonze, X. & Lee, C. Dynamical matrices, Born effective charges, dielectric permittivity tensors, and interatomic force constants from density-functional perturbation theory. *Phys. Rev. B*. **55**, 10355–10368 (1997).
41. Baroni, S., de Gironcoli, S., Dal Corso, A. & Giannozzi, P. Phonons and related crystal properties from density-functional perturbation theory. *Rev. Mod. Phys.* **73**, 515–562 (2001).
42. Dal Corso, A. Density-functional perturbation theory with ultrasoft pseudopotentials. *Phys. Rev. B*. **64**, 235118 (2001).
43. Oliveira, L. N., Gross, E. K. U. & Kohn, W. Density-functional theory for superconductors. *Phys. Rev. Lett.* **60**, 2430–2433 (1988).
44. Lüders, M. et al. Ab initio theory of superconductivity. I. Density functional formalism and approximate functionals. *Phys. Rev. B*. **72**, 024545 (2005).
45. Marques, M. A. L. et al. Ab initio theory of superconductivity. II. Application to elemental metals. *Phys. Rev. B*. **72**, 024546 (2005).
46. Sanna, A., Pellegrini, C. & Gross, E. K. U. Combining Eliashberg theory with density functional theory for the accurate prediction of superconducting transition temperatures and gap functions. *Phys. Rev. Lett.* **125**, 057001 (2020).
47. Choudhary, K. & Garrity, K. Designing high-T_C superconductors with BCS-inspired screening, density functional theory, and deep-learning. *Npj Comput. Mater.* **8**, 244 (2022).
48. Xie, S. R. et al. Machine learning of superconducting critical temperature from Eliashberg theory. *Npj Comput. Mater.* **8**, 14 (2022).
49. Cerqueira, T. F. T., Sanna, A. & Marques, M. A. L. Sampling the materials space for conventional superconducting compounds. *Adv. Mater.* **36**, 2307085 (2024).
50. Gibson, J. B. et al. Accelerating superconductor discovery through tempered deep learning of the electron-phonon spectral function. *Npj Comput. Mater.* **11**, 7 (2025).
51. Gibson, J. B. et al. Developing a complete AI-accelerated workflow for superconductor discovery. *Npj Comput. Mater.* **12**, 95 (2026).
52. Nepal, N. K. & Wang, L.-L. Machine-learning guided search for phonon-mediated superconductivity in boron and carbon compounds. *Npj Comput. Mater.* **12**, 152 (2026).
53. Kolmogorov, A. N., Calandra, M. & Curtarolo, S. Thermodynamic stabilities of ternary metal borides: An ab initio guide for synthesizing layered superconductors. *Phys. Rev. B*. **78**, 094520 (2008).
54. Rodriguez, C. O. et al. Optical near-zone-center phonons and their interaction with electrons in $YBa_2Cu_3O_7$: Results of the local-density approximation. *Phys. Rev. B*. **42**, 2692–2695 (1990).
55. Sun, Y. et al. Electron-phonon coupling strength from ab initio frozen-phonon approach. *Phys. Rev. Mater.* **6**, 074801 (2022).
56. Dicks, O. A., Foyevtsova, K., Elfimov, I., Prasankumar, R. P. & Sawatzky, G. Computationally efficient method for calculating electron-phonon coupling for high-throughput superconductivity screening. *Phys. Rev. B*. **110**, 184517 (2024).
57. di Mauro, M. E., Braïda, B., Errea, I., Novoa, T. & Contreras-García, J. Molecularity: A fast and efficient criterion for probing superconductivity. *Phys. Rev. B*. **110**, 174515 (2024).
58. Belli, F., Torres, S., Contreras-Garcìa, J. & Zurek, E. Refining T_c prediction in hydrides via symbolic-regression-enhanced electron-localization-function-based descriptors. *Ann. Phys.* **537**, e00280 (2025).
59. Novoa, T., Bianco, R., Contreras-García, J. & Errea, I. Real-space understanding of electron-phonon coupling in superconducting hydrides. Preprint at https://doi.org/10.48550/arXiv.2507.06749 (2025).
60. Maksimov, E. Self-consistent description of electron-phonon system in metals and problem of lattice stability. *Zh. Éksp. Teor. Fiz.* **69**, 2236–2248 (1975).
61. McMillan, W. L. Transition temperature of strong-coupled superconductors. *Phys. Rev.* **167**, 331–344 (1968).
62. Hopfield, J. J. Angular momentum and transition-metal superconductivity. *Phys. Rev.* **186**, 443–451 (1969).
63. Loew, A., Sun, D., Wang, H.-C., Botti, S. & Marques, M. A. L. Universal machine learning interatomic potentials are ready for phonons. *Npj Comput. Mater.* **11**, 178 (2025).

64. Anam, M. Z. et al. A comprehensive assessment and benchmark study of large atomistic foundation models for phonons. *Adv. Intell. Discov.* e202500075, https://doi.org/10.1002/aidi.202500075 (2025).
65. Fu, X. et al. Learning smooth and expressive interatomic potentials for physical property prediction. Preprint at https://doi.org/10.48550/arXiv.2502.12147 (2025).
66. Marcial, E. T., Chaudhary, L., Gorbunova, O. & Kolmogorov, A. N. Performance of universal machine learning potentials in global optimization. Preprint at https://doi.org/10.48550/arXiv.2602.23515 (2026).
67. Mazin, I. I., Rashkeev, S. N. & Savrasov, S. Y. Nonspherical rigid-muffin-tin calculations of electron-phonon coupling in high-T_c perovskites. *Phys. Rev. B*. **42**, 366–370 (1990).
68. Papaconstantopoulos, D. A., Mehl, M. J. & Economou, E. N. High-temperature superconductivity in the Ca-Sc-H system. *Phys. Rev. B*. **108**, 224508 (2023).
69. Foulkes, I. F. & Gomersall, I. R. A simple theory of the phonon contribution to the electron-phonon mass enhancement. *J. Phys. F: Met. Phys.* **5**, 153 (1975).
70. Ashcroft, N. W., Mermin, N. *Solid State Physics* (Brooks/Cole, 1976).
71. Kittel, C. *Introduction to Solid State Physics* 8th edn (John Wiley & Sons, New York, 2004).
72. Quan, Y., Ghosh, S. S. & Pickett, W. E. Compressed hydrides as metallic hydrogen superconductors. *Phys. Rev. B*. **100**, 184505 (2019).
73. Quan, Y., Lee, K.-W. & Pickett, W. E. MoB_2 under pressure: Superconducting Mo enhanced by boron. *Phys. Rev. B*. **104**, 224504 (2021).
74. Kleinman, L. & Bylander, D. M. Efficacious form for model pseudopotentials. *Phys. Rev. Lett.* **48**, 1425–1428 (1982).
75. Bylander, D. M. & Kleinman, L. 4f resonances with norm-conserving pseudopotentials. *Phys. Rev. B*. **41**, 907–912 (1990).
76. Vanderbilt, D. Soft self-consistent pseudopotentials in a generalized eigenvalue formalism. *Phys. Rev. B*. **41**, 7892–7895 (1990).
77. Hamann, D. R., Schlüter, M. & Chiang, C. Norm-conserving pseudopotentials. *Phys. Rev. Lett.* **43**, 1494–1497 (1979).
78. Hamann, D. R. Optimized norm-conserving Vanderbilt pseudopotentials. *Phys. Rev. B*. **88**, 085117 (2013).
79. Gonze, X., Stumpf, R. & Scheffler, M. Analysis of separable potentials. *Phys. Rev. B*. **44**, 8503–8513 (1991).
80. Rabinowitz, P. & Davis, P. J. *Methods of numerical integration*. Dover Books on Mathematics, 2 edn (Dover Publications, 2007).
81. Kortus, J., Mazin, I. I., Belashchenko, K. D., Antropov, V. P. & Boyer, L. L. Superconductivity of metallic boron in MgB_2. *Phys. Rev. Lett.* **86**, 4656–4659 (2001).
82. Dynes, R. Mcmillan's equation and the T_c of superconductors. *Solid State Commun.* **10**, 615–618 (1972).
83. Karakozov, A., Maksimov, E. & Mashkov, S. Effect of frequency-dependence of electron-phonon interaction spectral-function on thermodynamic properties of superconductors. *Zh.Éksp. Teor. Fiz.* **68**, 1937–1950 (1975)..
84. Allen, P. B. & Dynes, R. C. Transition temperature of strong-coupled superconductors reanalyzed. *Phys. Rev. B*. **12**, 905–922 (1975).
85. Ginzburg, V. & Kirzhnits, D. On the problem of high temperature superconductivity. *Phys. Rep.* **4**, 343–356 (1972).
86. Bogoljubov, N. N. On a new method in the theory of superconductivity. *Il Nuovo Cim.* **7**, 794–805 (1958).
87. Zehder, R. C. & Winter, H. On the influence of spin fluctuations on the superconducting transition temperatures of transition metals. *J. Phys. Condens. Matter* **2**, 7479 (1990).
88. Schrieffer, J. R. *Theory of superconductivity* (Perseus Books, 1999).
89. Hermann, C., Ewald, P. P. Strukturbericht 1913-1928 : Zeitschrift für Kristallographie, Kristallgeometrie, Kristallgeometrie, Kristallphysik, Kristallchemie, Ergänzungsband. Akademische Verlagsgesellschaft: Leipzig, 1931.
90. Savrasov, S. Y. & Savrasov, D. Y. Electron-phonon interactions and related physical properties of metals from linear-response theory. *Phys. Rev. B*. **54**, 16487–16501 (1996).
91. Takezawa, T., Nagara, H. & Suzuki, N. Ab initio calculations of superconductivity in palladium under pressure. *Phys. Rev. B*. **71**, 012515 (2005).
92. Isaev, E. I. et al. Phonon related properties of transition metals, their carbides, and nitrides: A first-principles study. *J. Appl. Phys.* **101**, 123519 (2007).
93. Tütüncü, H., Uzunok, H., Srivastava, G., Özdemir, V. & Uğur, G. The effect of martensitic phase transition from cubic to tetragonal on the physical properties of V_3Si superconductor. *Intermetallics* **96**, 25–32 (2018).
94. Sauer, A. et al. Electron-phonon coupling and superconductivity-induced distortion of the phonon lineshape in V_3Si. *Phys. Rev. B*. **99**, 134511 (2019).
95. Wierzbowska, M., de Gironcoli, S. & Giannozzi, P. Origins of low- and high-pressure discontinuities of T_c in niobium. Preprint at https://doi.org/10.48550/arXiv.cond-mat/0504077 (2006).
96. Rietschel, H. & Winter, H. Role of spin fluctuations in the superconductors Nb and V. *Phys. Rev. Lett.* **43**, 1256–1260 (1979).
97. Tsutsumi, K., Hizume, Y., Kawamura, M., Akashi, R. & Tsuneyuki, S. Effect of spin fluctuations on superconductivity in V and Nb: A first-principles study. *Phys. Rev. B*. **102**, 214515 (2020).
98. Jones, D. et al. Superconducting transition temperatures of pure vanadium and vanadium-titanium alloys in the presence of dynamical electronic correlations. *Phys. Rev. B*. **109**, 165107 (2024).
99. Giannozzi, P. et al. QUANTUM ESPRESSO: a modular and open-source software project for quantum simulations of materials. *J. Phys. Condens. Matter* **21**, 395502 (2009).
100. Giannozzi, P. et al. Advanced capabilities for materials modelling with Quantum ESPRESSO. *J. Phys. Condens. Matter* **29**, 465901 (2017).
101. Giannozzi, P. et al. Quantum ESPRESSO toward the exascale. *J. Chem. Phys.* **152**, 154105 (2020).
102. Bai, Z., Bhullar, M., Akinpelu, A. & Yao, Y. Unveiling future superconductors through machine learning. *Mater. Today Phys.* **43**, 101384 (2024).
103. Perdew, J. P., Burke, K. & Ernzerhof, M. Generalized gradient approximation made simple. *Phys. Rev. Lett.* **77**, 3865–3868 (1996).
104. Methfessel, M. & Paxton, A. T. High-precision sampling for Brillouin-zone integration in metals. *Phys. Rev. B*. **40**, 3616–3621 (1989).
105. Blöchl, P. E., Jepsen, O. & Andersen, O. K. Improved tetrahedron method for Brillouin-zone integrations. *Phys. Rev. B*. **49**, 16223–16233 (1994).
106. Weinert, M., Schneider, G., Podloucky, R. & Redinger, J. FLAPW: applications and implementations. *J. Phys. Condens. Matter* **21**, 084201 (2009).
107. Togo, A., Chaput, L., Tadano, T. & Tanaka, I. Implementation strategies in phonopy and phono3py. *J. Phys. Condens. Matter* **35**, 353001 (2023).
108. Togo, A. First-principles phonon calculations with phonopy and phono3py. *J. Phys. Soc. Jpn.* **92**, 012001 (2023).
109. Kresse, G. & Hafner, J. Ab initio molecular dynamics for liquid metals. *Phys. Rev. B*. **47**, 558–561 (1993).
110. Kresse, G. & Hafner, J. Ab initio molecular-dynamics simulation of the liquid-metal–amorphous-semiconductor transition in germanium. *Phys. Rev. B*. **49**, 14251–14269 (1994).
111. Kresse, G. & Furthmüller, J. Efficient iterative schemes for ab initio total-energy calculations using a plane-wave basis set. *Phys. Rev. B*. **54**, 11169–11186 (1996).
112. Kresse, G. & Furthmüller, J. Efficiency of ab-initio total energy calculations for metals and semiconductors using a plane-wave basis set. *Comput. Mater. Sci.* **6**, 15–50 (1996).

113. Kresse, G. & Joubert, D. From ultrasoft pseudopotentials to the projector augmented-wave method. *Phys. Rev. B*. **59**, 1758–1775 (1999).
114. Souvatzis, P. & Eriksson, O. Ab initio calculations of the phonon spectra and the thermal expansion coefficients of the 4*d* metals. *Phys. Rev. B*. **77**, 024110 (2008).
115. Texas Advanced Computing Center (TACC). Service provided by the University of Texas at Austin, http://www.tacc.utexas.edu.
116. Stanzione, D. et al. *Frontera: The Evolution of Leadership Computing at the National Science Foundation*, 106–111 (ACM, 2020).

Acknowledgements

This work was supported by the National Science Foundation (Grants No. DMR-2320074, DMR-2320073, and DMREF-2323857). Computational resources were provided by the Texas Advanced Computing Center (TACC) at The University of Texas at Austin[115], specifically the Frontera[116] supercomputer, through Allocation DMR22004. Frontera is supported by NSF Award OAC-1818253.

Author contributions

I.I.M., A.N.K. and E.R.M. conceived the project. D.R., I.I.M., T.S. and M.W. contributed to the development of the analytical RMTA methodology for PP + PW codes through discussions. D.R., T.S. and M.W. carried out all software development. D.R. derived the final form of the RMTA equations for PP+PW codes, wrote a postprocessing RMTA code for calculating the MH parameters, compatible with QE PW, and performed the corresponding calculations. T.S. and M.W. produced reference MH parameters with the FLAPW method. A.N.K. and D.R. performed the ionic factor analysis. D.R., E.R.M., A.N.K. and I.I.M. wrote the manuscript. All authors reviewed the manuscript and provided comments.

Competing interests

The authors declare no competing interests.

Additional information

Supplementary information The online version contains supplementary material available at https://doi.org/10.1038/s41524-026-02141-7.

Correspondence and requests for materials should be addressed to Danylo Radevych.

Rigid muffin-tin approximation in plane-wave codes for fast modeling of phonon-mediated superconductors
Supplementary Information

Danylo Radevych,[1,*] Tatsuya Shishidou,[2] Michael Weinert,[2]
Elena R. Margine,[3] Aleksey N. Kolmogorov,[3] and Igor I. Mazin[1,4]

[1] *Department of Physics and Astronomy, George Mason University, Fairfax, VA 22030, USA*
[2] *Department of Physics, University of Wisconsin-Milwaukee, Milwaukee, WI 53201, USA*
[3] *Department of Physics, Applied Physics and Astronomy, Binghamton University-SUNY, Binghamton, New York 13902, USA*
[4] *Quantum Science and Engineering Center, George Mason University, Fairfax, VA 22030, USA*

ASSUMPTIONS OF SPHERICAL POTENTIAL AND BANDS FOR MCMILLAN-HOPFIELD PARAMETERS

This section demonstrates how the assumptions of a spherical potential and spherical bands lead to simplified expressions for the McMillan-Hopfield (MH) parameters. Following [1–3], Eq. (9) of the main text can be rewritten as

$$\begin{aligned}\tilde{\eta}_\kappa = \frac{\Omega^2}{(2\pi)^6 N(\varepsilon_\mathrm{F})} \sum_{ij}^{N_\mathrm{states}} \int_\mathrm{BZ} d\boldsymbol{k}\delta\left(\varepsilon_{i,\boldsymbol{k}} - \varepsilon_\mathrm{F}\right) \int_\mathrm{BZ} d\boldsymbol{k}'\delta\left(\varepsilon_{j,\boldsymbol{k}'} - \varepsilon_\mathrm{F}\right) \int_\mathrm{MT} d\boldsymbol{r} \int_\mathrm{MT} d\boldsymbol{r}' \\ \times \Psi_{j,\boldsymbol{k}'}(\boldsymbol{r}')\Psi^*_{i,\boldsymbol{k}}(\boldsymbol{r}')\Psi^*_{j,\boldsymbol{k}'}(\boldsymbol{r})\Psi_{i,\boldsymbol{k}}(\boldsymbol{r})\left(\hat{\boldsymbol{r}}\cdot\hat{\boldsymbol{r}}'\right)\frac{dV_\kappa(r)}{dr}\frac{dV_\kappa(r')}{dr'}.\end{aligned} \tag{1}$$

While the explicit use of the wavefunction expansion from Eq. (14) of the main text would lead to four distinct sets of $\{l, m\}$ quantum numbers, corresponding to each wavefunction, the adoption of the spherical approximation in Eq. (15) of the main text and the orthonormality of the $\hat{\boldsymbol{k}}$- and $\hat{\boldsymbol{k}}'$-dependent spherical harmonics reduce the number of independent angular momentum indices to two sets: $\{l, m\}$ and $\{l', m'\}$. As a result, Eq. (1) simplifies to

$$\begin{aligned}\tilde{\eta}_\kappa = \frac{\Omega^2}{(2\pi)^6 N(\varepsilon_\mathrm{F})} \sum_{ij}^{N_\mathrm{states}} \sum_{lm}\sum_{l'm'} \int dk k^2 |a_{i\kappa,l}(k)|^2 \delta\left(\varepsilon_{i,\boldsymbol{k}} - \varepsilon_\mathrm{F}\right) \int dk'(k')^2 |a_{j\kappa,l'}(k')|^2 \delta\left(\varepsilon_{j,\boldsymbol{k}'} - \varepsilon_\mathrm{F}\right) \\ \times \left|\int_0^{r_{\kappa,\mathrm{MT}}} dr r^2 R_{\kappa,l}(r,\varepsilon_\mathrm{F})\frac{dV_\kappa(r)}{dr}R_{\kappa,l'}(r,\varepsilon_\mathrm{F})\right|^2 \int d\hat{\boldsymbol{r}} \int d\hat{\boldsymbol{r}}' Y_{lm}(\hat{\boldsymbol{r}})Y^*_{l'm'}(\hat{\boldsymbol{r}})Y^*_{lm}(\hat{\boldsymbol{r}}')Y_{l'm'}(\hat{\boldsymbol{r}}')\left(\hat{\boldsymbol{r}}\cdot\hat{\boldsymbol{r}}'\right).\end{aligned} \tag{2}$$

The next simplification is achieved by taking advantage of the separation of the spatial dependence of $\boldsymbol{r}$ into radial, r, and angular, $\hat{\boldsymbol{r}}$, components. Applying the identity [4]

$$\left(\hat{\boldsymbol{r}}\cdot\hat{\boldsymbol{r}}'\right) = \frac{4\pi}{3}\sum_{m''=-1}^{1} Y^*_{1m''}(\hat{\boldsymbol{r}}')Y_{1m''}(\hat{\boldsymbol{r}}), \tag{3}$$

along with the properties of Gaunt coefficients (integrals involving three spherical harmonics [5]), Eq. (2) simplifies to a form involving only dipole transitions with $l' = l \pm 1$ and $m' = m + m''$. The resulting expression for $\tilde{\eta}_\kappa$ is given by Eqs. (16)–(18) of the main text.

Notably, the partial electronic density of states (eDOS), defined in Eq. (17), can be further simplified by using the normalization of the radial functions in Eq. (8):

$$\begin{aligned}n_{\kappa,l}(r_{\kappa,\mathrm{MT}};\varepsilon_\mathrm{F}) &= \sum_m n_{\kappa,lm}(r_{\kappa,\mathrm{MT}};\varepsilon_\mathrm{F}) \\ &= \sum_m \frac{\Omega r_{\kappa,\mathrm{MT}}}{(2\pi)^3}\left(-R^2_{\kappa,l}\frac{\partial L_{\kappa,l}}{\partial\varepsilon}\bigg|_{\substack{r=r_{\kappa,\mathrm{MT}}\\ \varepsilon=\varepsilon_\mathrm{F}}}\right)\sum_i \int_\mathrm{BZ} d\boldsymbol{k}\delta(\varepsilon_{i,\boldsymbol{k}} - \varepsilon_\mathrm{F})\left|a_{i\kappa,lm}(\boldsymbol{k})\right|^2.\end{aligned} \tag{4}$$

* Corresponding author: dradevyc@gmu.edu

In Eq. (4), the integrals over r are replaced by energy derivatives of the logarithmic derivatives, $\partial L_{\kappa,l}/\partial\varepsilon$, evaluated only on the surface of the muffin-tin (MT) sphere.

NORMALIZATION OF THE RADIAL FUNCTIONS

The radial Schrödinger equation [Eq. (22) of the main text] for the l-channel can be rewritten as

$$-\frac{1}{r^2}\frac{\partial}{\partial r}\left(r^2\frac{\partial R_{\kappa,l}(r,\varepsilon)}{\partial r}\right)+\frac{l\,(l+1)}{r^2}R_{\kappa,l}(r,\varepsilon)+V_\kappa(r)R_{\kappa,l}(r,\varepsilon)=\varepsilon R_{\kappa,l}(r,\varepsilon). \tag{5}$$

The energy derivative of this equation is given by

$$-\frac{1}{r^2}\frac{\partial}{\partial r}\left(r^2\frac{\partial^2 R_{\kappa,l}}{\partial\varepsilon\partial r}\right)+\frac{l\,(l+1)}{r^2}\frac{\partial R_{\kappa,l}}{\partial\varepsilon}+V_\kappa\frac{\partial R_{\kappa,l}}{\partial\varepsilon}=R_{\kappa,l}+\varepsilon\frac{\partial R_{\kappa,l}}{\partial\varepsilon}. \tag{6}$$

Multiplying Eq. (5) by $\partial R_{\kappa,l}/\partial\varepsilon$, Eq. (6) by $R_{\kappa,l}$, and taking the difference between the two yields the following identity:

$$r^2R_{\kappa,l}^2=\frac{\partial}{\partial r}\left[r^2\left(\frac{\partial R_{\kappa,l}}{\partial\varepsilon}\frac{\partial R_{\kappa,l}}{\partial r}-R_{\kappa,l}\frac{\partial^2 R_{\kappa,l}}{\partial r\partial\varepsilon}\right)\right]. \tag{7}$$

Integrating both sides of Eq. (7) over r from 0 to $r_{\kappa,\mathrm{MT}}$ allows the normalization integral of the radial function to be expressed in terms of the energy derivative of the logarithmic derivative of this function as

$$\int_0^{r_{\kappa,\mathrm{MT}}}drr^2R_{\kappa,l}^2(r,\varepsilon)=r_{\kappa,\mathrm{MT}}^2\left(\frac{\partial R_{\kappa,l}}{\partial\varepsilon}\frac{\partial R_{\kappa,l}}{\partial r}-R_{\kappa,l}\frac{\partial^2 R_{\kappa,l}}{\partial r\partial\varepsilon}\right)\Bigg|_{r=r_{\kappa,\mathrm{MT}}}=-r_{\kappa,\mathrm{MT}}R_{\kappa,l}^2\frac{\partial L_{\kappa,l}}{\partial\varepsilon}\Bigg|_{r=r_{\kappa,\mathrm{MT}}}, \tag{8}$$

where the final equality follows from the definition of the logarithmic derivative, $L_{\kappa,l}$.

LOCAL SCREENED ATOMIC POTENTIAL

The coefficients $\tilde{V}(\boldsymbol{G})$ in the plane-wave expansion of the periodic local screened potential $V_{\mathrm{loc}}(\boldsymbol{r}_0)$ [Fig. 3b] are given by Eq. (20) of the main text, where the vector $\boldsymbol{r}_0$ starts at the origin of the calculated periodic unit cell [see Fig. 3a]. To obtain the periodic local potential on the atom-centered $\boldsymbol{r}$-grid, with the atom located at $\boldsymbol{\tau}_\kappa$, such that $\boldsymbol{r}_0=\boldsymbol{\tau}_\kappa+\boldsymbol{r}$, one can apply the inverse Fourier transform

$$\begin{aligned}V_{\kappa,\mathrm{loc}}(\boldsymbol{r})=V_{\mathrm{loc}}(\boldsymbol{r}_0)=V_{\mathrm{loc}}(\boldsymbol{\tau}_\kappa+\boldsymbol{r})&=\sum_{\boldsymbol{G}}\left[e^{i\boldsymbol{G}\cdot\boldsymbol{\tau}_\kappa}\tilde{V}(\boldsymbol{G})\right]e^{i\boldsymbol{G}\cdot\boldsymbol{r}}\\&=4\pi\sum_{\boldsymbol{G}}\left[e^{i\boldsymbol{G}\cdot\boldsymbol{\tau}_\kappa}\tilde{V}(\boldsymbol{G})\right]\sum_{l,m}i^l j_l(Gr)Y_{lm}^*(\hat{\boldsymbol{G}})Y_{lm}(\hat{\boldsymbol{r}}).\end{aligned} \tag{9}$$

In the final equality of Eq. (9), the plane wave $e^{i\boldsymbol{G}\cdot\boldsymbol{r}}$ was expanded in terms of spherical harmonics Y_{lm} and spherical Bessel functions j_l. If only the spherically symmetric terms corresponding to $l=m=0$ are kept, Eq. (9) simplifies to the spherically-symmetric atomic potential given in Eq. (21) of the main text.

SEMILOCAL AND NON-LOCAL PARTS OF HAMANN PSEUDOPOTENTIALS

For the atom κ, the total non-local Vanderbilt-Kleinman-Bylander (NL-VKB) [6–8] pseudopotential corresponding to angular momentum l is generally written as

$$V_{\kappa,\mathrm{tot}}^l(r,r')=V_{\kappa,\mathrm{loc}}(r)+V_{\kappa,\mathrm{NL}}^l(r,r')=V_{\kappa,\mathrm{loc}}(r)+\sum_{ij\in\{l\}}D_{\kappa,ij}\beta_{\kappa,i}(r)\beta_{\kappa,j}(r'), \tag{10}$$

where $V^l_{\kappa,\mathrm{NL}}(r,r')$ is the fully non-local part that includes only the beta-projectors $\beta_{\kappa,i}(r)$ and $\beta_{\kappa,j}(r)$ generated for angular momentum l. These projectors are read directly from the pseudopotential file along with the normalization coefficients $D_{\kappa,ij}$. The local part $V_{\kappa,\mathrm{loc}}(r)$ is extracted from a density-functional theory (DFT) calculation. With fully non-local pseudopotentials, the radial Schrödinger equation for the radial functions is

$$-\frac{d^2}{dr^2}\left[rR_{\kappa,l}(r,\varepsilon)\right] + \int dr' V^l_{\kappa,\mathrm{tot}}(r,r')\left[r'R_{\kappa,l}(r',\varepsilon)\right] = \varepsilon\left[rR_{\kappa,l}(r,\varepsilon)\right]. \tag{11}$$

While Eq. (11) can be solved numerically, in some cases it is more straightforward to convert the non-local pseudopotential to a semilocal (SL) form, if such a conversion is possible. The non-local Hamann optimized norm-conserving Vanderbilt pseudopotentials (ONCVPSP) [9, 10], used in the present work, allow for this conversion, as the pseudopotential files include the radial functions $\chi_{\kappa,l}(r) = rR_{\kappa,l}(r)$, evaluated at the same reference energies used to construct the beta-projectors. With these radial functions, the semilocal components of the potential can be reconstructed as

$$V^l_{\kappa,\mathrm{SL}}(r) = \frac{1}{\chi_{\kappa,l}(r)} \sum_{ij\in\{l\}} D_{\kappa,ij}\beta_{\kappa,i}(r) \int dr' \beta_{\kappa,j}(r')\chi_{\kappa,l}(r'). \tag{12}$$

Alternatively, since the Hamann ONCVPSP code computes the SL parts internally, they can be printed directly in the pseudopotential file and read from there. In our tests, the SL parts calculated with Eq. (12) were found to be identical to those printed directly by the Hamann ONCVPSP code.

CRYSTALLOGRAPHIC PARAMETERS

The crystallographic parameters of all the structures used in this work are reported in Table S1.

TABLE S1. **Crystallographic parameters of the considered structures.**

Structure	Space group	$a=b=c$ (bohr)	$\alpha=\beta=\gamma$ (°)	Atom	x, y, z (crystal units)	Wyckoff position
bcc-V	$Im\bar{3}m$	5.72	90	V	0, 0, 0	2a
bcc-Nb	$Im\bar{3}m$	6.24	90	Nb	0, 0, 0	2a
bcc-Mo	$Im\bar{3}m$	5.95	90	Mo	0, 0, 0	2a
fcc-Pd	$Fm\bar{3}m$	7.54	90	Pd	0, 0, 0	4a
$A15$-V_3Sn	$Pm\bar{3}n$	9.42	90	V	1/4, 1/2, 0	6d
				Sn	0, 0, 0	2a
$A15$-V_3Si	$Pm\bar{3}n$	8.93	90	V	1/4, 1/2, 0	6d
				Si	0, 0, 0	2a
$A15$-Nb_3Si	$Pm\bar{3}n$	10.07	90	Nb	1/4, 1/2, 0	6d
				Si	0, 0, 0	2a
$L1_2$-Nb_3Si	$Pm\bar{3}m$	7.97	90	Nb	0, 1/2, 1/2	3c
				Si	0, 0, 0	1a
$B1$-NbN	$Fm\bar{3}m$	8.29	90	Nb	1/2, 1/2, 1/2	4b
				N	0, 0, 0	4a

SMEARING VS. TETRAHEDRON INTEGRATION METHODS

The convergence of the total and partial eDOS at the Fermi level with respect to the uniform $\boldsymbol{k}$-grid size is crucial to obtain reliable McMillan-Hopfield parameters. As shown in Figure S1a,b, the convergence of the McMillan-Hopfield parameter for bcc-Nb closely follows that of the eDOS. When the tetrahedron integration method is used to evaluate the delta-function integrals in the eDOS expressions in Eqs. (26) and (27) of the main text, the results converge significantly faster [orange lines in Figure S1a,b] than when the same smearing is used to approximate the occupation function in the self-consistent field (SCF) calculation and the delta-function in the eDOS part [black and gray lines in Figure S1a,b]. Consequently, the tetrahedron integration method is used by default in all rigid muffin-tin approximation (RMTA) calculations presented here.

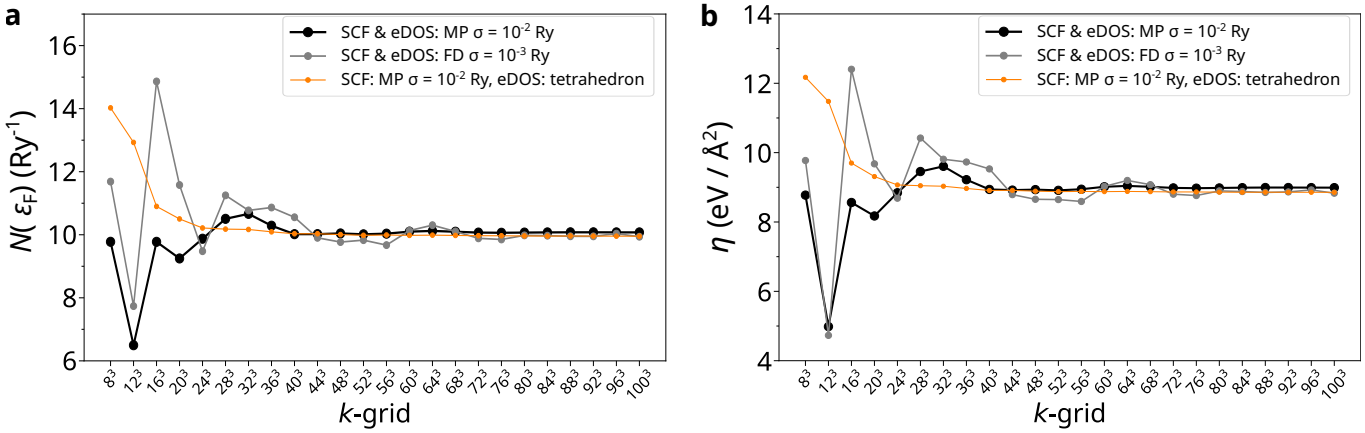

FIG. S1. **Convergence of the electronic density of states at the Fermi level and the McMillan–Hopfield parameter. a** Electronic density of states (eDOS) at the Fermi level and **b** the McMillan–Hopfield parameter (η) as functions of the uniform $\boldsymbol{k}$-grid size for bcc-Nb. The abbreviations "MP" and "FD" represent Methfessel-Paxton and Fermi-Dirac smearing, respectively, with σ indicating the corresponding degauss value. In all cases, smearing is used to approximate the occupation function in the self-consistent field (SCF) calculations. In the subsequent RMTA calculation, the eDOS at the Fermi level converges faster when the tetrahedron method is used (orange lines) than when the delta-function is approximated by smearing (black and gray lines).

COMPARISON OF MCMILLAN-HOPFIELD PARAMETERS WITH PREVIOUS AUGMENTED PLANE-WAVE RESULTS

In Figure S2, the present McMillan-Hopfield parameters for the metal atoms in selected simple metals and compounds are compared with the results reported by Papaconstantopoulos *et al.* [11] and Pickett [12], obtained using the augmented plane-wave (APW) method with touching MT spheres. Our values agree well with those of Papaconstantopoulos *et al.* and Pickett for the simple metals, and are also reasonably close to Pickett's values for the binary compounds V_3Sn, V_3Si, and NbN. By contrast, Pickett's value for $A15$-Nb_3Si is significantly smaller than ours. This difference may arise from several technical factors, including differences in crystallographic parameters, all-electron potentials, exchange-correlation functionals, and possibly the treatment of the Nb semicore states as either core or valence in the APW method. Given the limited technical details provided in Ref. [12], it is difficult to identify the exact origin of the discrepancy. Nevertheless, all results are valid within the respective computational frameworks in which they were obtained.

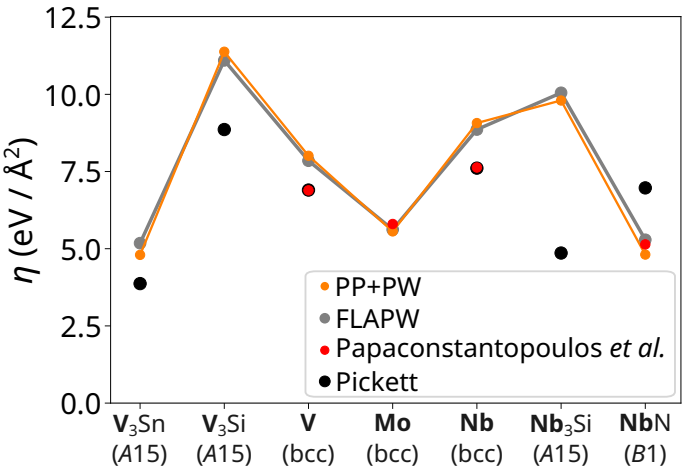

FIG. S2. **Comparison of calculated McMillan-Hopfield parameters with literature augmented plane-wave results.** Calculated parameters for V, Mo, and Nb atoms across various structures. Results from pseudopotential-based plane-wave (PP+PW) calculations (orange circles) and full-potential linearized augmented plane-wave (FLAPW) calculations (gray circles) are compared with literature values (red and black circles) obtained via the augmented plane-wave (APW) method as reported by Papaconstantopoulos *et al.* [11] and Pickett [12].

COMPARISON OF THE FINITE-DISPLACEMENT RESULTS OBTAINED WITH VASP PAW PBE PSEUDOPOTENTIALS AND UNIVERSAL MACHINE LEARNING POTENTIALS

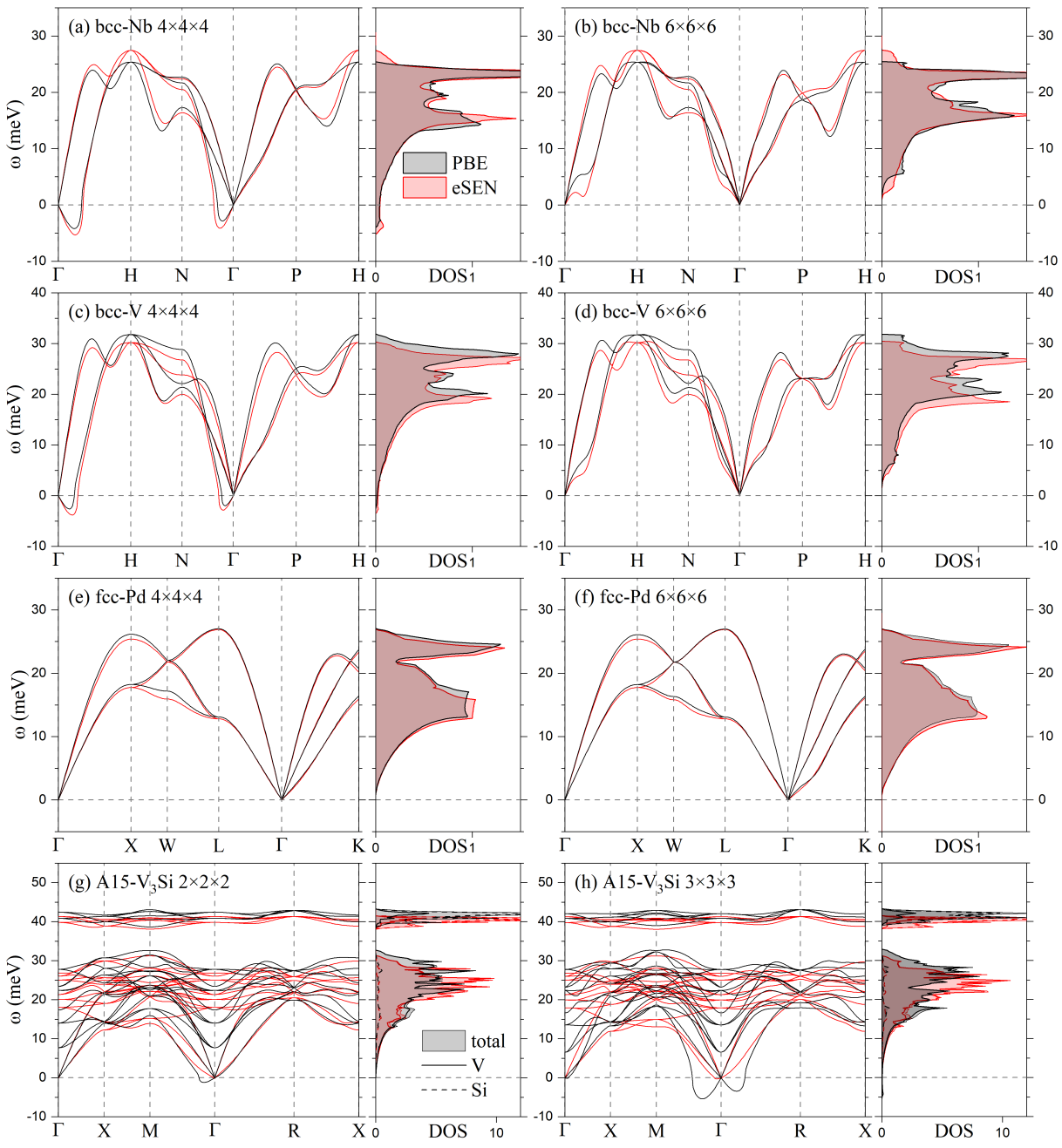

FIG. S3. **Comparison of phonon dispersions and density of states (DOS in states/meV per primitive unit cell) calculated with PBE and eSEN for elemental (bcc-Nb, bcc-V, and fcc-Pd) and binary ($A15$-V_3Si) materials.** **a** bcc-Nb 4×4×4, **b** bcc-Nb 6×6×6, **c** bcc-V 4×4×4, **d** bcc-V 6×6×6, **e** fcc-Pd 4×4×4, **f** fcc-Pd 6×6×6, **g** $A15$-V_3Si 2×2×2, and **h** $A15$-V_3Si 3×3×3. We employed Phonopy to set up and post-process finite-displacement calculations with a 0.1 Å shift in supercells with either 64 atoms (a,c,e,g) or 216 atoms (b,d,f,h). The PBE analysis was performed with Vienna *ab initio* simulation package (VASP) using a 500-eV energy cutoff and Monkhorst-Pack $\boldsymbol{k}$-meshes of $6 \times 6 \times 6$ and $4 \times 4 \times 4$ for the 64-atom and 216-atom supercells, respectively. The DOS integration was carried out on $20 \times 20 \times 20$ $\boldsymbol{q}$-point meshes, with the plots for the binary compound showing both total and atom-projected values.

TABLE S2. **Comparison of the local trace $\tilde{\phi}_\kappa = \frac{1}{3}\mathbf{Tr}\left[(\Phi_{\kappa\kappa})^{-1}\right]$ (Å^2/eV) and the Einstein frequency $\omega_\kappa = \frac{1}{\sqrt{M_\kappa \tilde{\phi}_\kappa}}$ (meV) for the considered phases.** The trace is found in real space by inverting block-diagonal atomic parts of the force constant matrices. Technical details on the finite-displacement calculations are given in the caption of Figure S3.

Supercell (atoms)	Method	bcc-Nb		bcc-V		fcc-Pd		$A15$-V_3Si			
		ϕ_{Nb}	ω_{Nb}	ϕ_{V}	ω_{V}	ϕ_{Pd}	ω_{Pd}	ϕ_{V}	ω_{V}	ϕ_{Si}	ω_{Si}
64	eSEN	0.134	18.33	0.175	21.68	0.125	17.74	0.142	24.08	0.106	37.47
	PBE	0.134	18.35	0.159	22.72	0.121	18.04	0.134	24.71	0.101	38.47
216	eSEN	0.135	18.26	0.176	21.60	0.125	17.75	0.143	23.92	0.106	37.43
	PBE	0.137	18.15	0.158	22.82	0.121	18.02	0.136	24.53	0.100	38.50

IONIC FACTOR FROM LOCAL IONIC DISPLACEMENTS IN SUPERCELLS

The interatomic force constant (IFC) matrix in real space is defined as the second derivative of the total energy of the system E with respect to the atomic displacements $\Delta\boldsymbol{\tau}_\kappa^{\boldsymbol{l}}$ and $\Delta\boldsymbol{\tau}_{\kappa'}^{\boldsymbol{l}'}$ of atoms κ and κ' in their corresponding unit cells $\boldsymbol{l}$ and $\boldsymbol{l}'$:

$$\Phi_{\kappa\alpha\boldsymbol{l},\kappa'\beta\boldsymbol{l}'} = \frac{\partial^2 E}{\partial\tau_{\kappa\alpha}^{\boldsymbol{l}}\partial\tau_{\kappa'\beta}^{\boldsymbol{l}'}}. \tag{13}$$

In the local-vibration approximation, the local block of the IFC matrix $\Phi_{\kappa\kappa}$ is sufficient to calculate the ionic factor—$\tilde{\phi}_\kappa = \frac{1}{3}\mathrm{Tr}\left[(\Phi_{\kappa\kappa})^{-1}\right]$—of the atomic electron-phonon coupling (EPC) constant $\tilde{\lambda}_\kappa$. This block can be calculated from the forces acting on atoms in the supercells, by displacing the atom κ in the original unit cell $\mathbf{0}$, along each Cartesian direction as:

$$\Phi_{\kappa\kappa} = \begin{bmatrix} \frac{\partial^2 E}{\partial\tau_{\kappa x}^{\mathbf{0}\,2}} & \frac{\partial^2 E}{\partial\tau_{\kappa x}^{\mathbf{0}}\partial\tau_{\kappa y}^{\mathbf{0}}} & \frac{\partial^2 E}{\partial\tau_{\kappa x}^{\mathbf{0}}\partial\tau_{\kappa z}^{\mathbf{0}}} \\ \frac{\partial^2 E}{\partial\tau_{\kappa y}^{\mathbf{0}}\partial\tau_{\kappa x}^{\mathbf{0}}} & \frac{\partial^2 E}{\partial\tau_{\kappa y}^{\mathbf{0}\,2}} & \frac{\partial^2 E}{\partial\tau_{\kappa y}^{\mathbf{0}}\partial\tau_{\kappa z}^{\mathbf{0}}} \\ \frac{\partial^2 E}{\partial\tau_{\kappa z}^{\mathbf{0}}\partial\tau_{\kappa x}^{\mathbf{0}}} & \frac{\partial^2 E}{\partial\tau_{\kappa z}^{\mathbf{0}}\partial\tau_{\kappa y}^{\mathbf{0}}} & \frac{\partial^2 E}{\partial\tau_{\kappa z}^{\mathbf{0}\,2}} \end{bmatrix} = -\begin{bmatrix} \frac{\partial F_{\kappa,x}}{\partial\tau_{\kappa x}^{\mathbf{0}}} & \frac{\partial F_{\kappa,x}}{\partial\tau_{\kappa y}^{\mathbf{0}}} & \frac{\partial F_{\kappa,x}}{\partial\tau_{\kappa z}^{\mathbf{0}}} \\ \frac{\partial F_{\kappa,y}}{\partial\tau_{\kappa x}^{\mathbf{0}}} & \frac{\partial F_{\kappa,y}}{\partial\tau_{\kappa y}^{\mathbf{0}}} & \frac{\partial F_{\kappa,y}}{\partial\tau_{\kappa z}^{\mathbf{0}}} \\ \frac{\partial F_{\kappa,z}}{\partial\tau_{\kappa x}^{\mathbf{0}}} & \frac{\partial F_{\kappa,z}}{\partial\tau_{\kappa y}^{\mathbf{0}}} & \frac{\partial F_{\kappa,z}}{\partial\tau_{\kappa z}^{\mathbf{0}}} \end{bmatrix} = -\begin{bmatrix} \boldsymbol{\nabla}_\kappa F_{\kappa,x} \\ \boldsymbol{\nabla}_\kappa F_{\kappa,y} \\ \boldsymbol{\nabla}_\kappa F_{\kappa,z} \end{bmatrix}, \tag{14}$$

where $\boldsymbol{\nabla}_\kappa = \left(\partial/\partial\tau_{\kappa x}^{\mathbf{0}}, \partial/\partial\tau_{\kappa y}^{\mathbf{0}}, \partial/\partial\tau_{\kappa z}^{\mathbf{0}}\right)$, and $\boldsymbol{F}_\kappa = -\boldsymbol{\nabla}_\kappa E$ is the force acting on the atom κ when it is displaced from its equilibrium position $\boldsymbol{\tau}_\kappa^{\mathbf{0}}$ by a small vector $\Delta\boldsymbol{\tau}_\kappa^{\mathbf{0}}$. In Eq. (14), the matrix $\Phi_{\kappa\kappa}$ is symmetric, has six unique elements, and generally requires six numerical evaluations of $\boldsymbol{F}_\kappa$—specifically, two atomic displacements along each Cartesian axis:

$$\frac{\partial \boldsymbol{F}_\kappa(\boldsymbol{\tau}_\kappa^{\mathbf{0}})}{\partial\tau_{\kappa,\alpha}^{\mathbf{0}}} = \frac{\boldsymbol{F}_\kappa(\boldsymbol{\tau}_\kappa^{\mathbf{0}} + \Delta\tau_{\kappa,\alpha}^{\mathbf{0}}\hat{\boldsymbol{\alpha}}) - \boldsymbol{F}_\kappa(\boldsymbol{\tau}_\kappa^{\mathbf{0}} - \Delta\tau_{\kappa,\alpha}^{\mathbf{0}}\hat{\boldsymbol{\alpha}})}{2\Delta\tau_{\kappa,\alpha}^{\mathbf{0}}}, \tag{15}$$

where $\hat{\boldsymbol{\alpha}}$ is a unit vector along the corresponding axis.

The calculation of $\Phi_{\kappa\kappa}$ should be performed only for one atom of each symmetry type. Hence, in the $A15$ compounds considered, only two atoms must be displaced in the supercells. By using the symmetry of the system, fewer than 6 total displacements per atom may be sufficient. In simple metals, 2 displacements of one atom along any of the standard Cartesian axes are performed. In $A15$ compounds, four displacements along two axes are applied to one metal atom and only two displacements along one axis are needed for a non-metal atom.

Table S3 demonstrates the convergence of the ionic factor calculated in a series of SCF runs with locally displaced representative atoms for four selected materials. A 3×3×3 supercell containing 27 atoms appears to be optimal for simple metals. Displacements performed in the 2×2×2 supercell of V_3Si, which consists of 64 atoms, yield better converged results than those in the primitive cell with 8 atoms. For fast RMTA estimates, however, displacements in the 2×2×2 supercells of simple metals and the primitive cell of the $A15$ compound are sufficient, since they provide $\tilde{\phi}_\kappa$ estimates within 20% of the converged values.

In Table S3, the characteristic phonon energy ω_κ is approximated via the ionic factor $\tilde{\phi}_\kappa$ and the atomic mass M_κ as [13]:

$$\omega_\kappa = \sqrt{\langle\omega_\kappa^2\rangle} \approx \frac{1}{\sqrt{M_\kappa\tilde{\phi}_\kappa}}, \tag{16}$$

and the logarithmic average phonon energy is obtained following [13, 14]:

$$\omega_{\ln} = \prod_{\kappa}^{N_{\text{atoms}}} \omega_{\kappa}^{\frac{\tilde{\lambda}_{\kappa}}{\lambda}}. \tag{17}$$

TABLE S3. **Convergence of the ionic factors and type-resolved electron-phonon coupling constants with respect to displacement parameters.** The ionic factor, defined as $\tilde{\phi}_{\kappa} = \frac{1}{3}\text{Tr}[(\Phi_{\kappa\kappa})^{-1}]$, and the type-resolved electron-phonon coupling (EPC) constant λ_{ν} are shown for representative materials as functions of displacement length and supercell size. Calculations are performed using a series of SCF runs in the Quantum ESPRESSO (QE) PW package, with displacements of representative atoms $\Delta\tau^{\mathbf{0}}_{\kappa,\alpha}$ along each Cartesian axis. The same ONCVPSP pseudopotentials, smearing, and wavefunction energy cutoff used for the calculation of the electronic factor η_{ν} are retained. A $24 \times 24 \times 24$ $\boldsymbol{k}$-point grid is used for the primitive cells of the simple metals, while a $12 \times 12 \times 12$ grid is used for the $A15$ compound; $\boldsymbol{k}$-grids for the supercells are rescaled accordingly. Reference $\tilde{\phi}_{\kappa}^{\text{DFPT}}$, $\lambda_{\nu}^{\text{DFPT}}$, and $\omega_{\ln}^{\text{DFPT}}$ values are obtained in this work via QE density-functional perturbation theory (DFPT) calculations using identical parameters and $\boldsymbol{q}$-grids that correspond to the sizes of the equivalent finite-displacement supercells. $\kappa \in \{\nu\}$ is assumed.

Material	Type ν	$r_{\kappa,\text{MT}}$ (bohr)	η_{ν} (eV/Å^2)	$\Delta\tau^{\mathbf{0}}_{\kappa,\alpha}$ (Å)	Supercell / $\boldsymbol{q}$-grid	N_{atoms}	$\tilde{\phi}_{\kappa}$ (Å^2/eV)	$\tilde{\phi}_{\kappa}^{\text{DFPT}}$ (Å^2/eV)	λ_{ν}	λ	λ^{DFPT}	ω_{κ} (K)	$\omega_{\ln}$ (K)	$\omega_{\ln}^{\text{DFPT}}$ (K)
bcc-V	V	2.48	8.01	0.01	2×2×2	8	0.157	0.157	1.26	1.26	1.37	266	266	240
					3×3×3	27	0.183	0.183	1.47	1.47	1.17	246	246	244
					4×4×4	64	0.179	0.179	1.43	1.43	1.30	249	249	227
					6×6×6	216	0.180	0.180	1.44	1.44	1.53	248	248	185
				0.10	2×2×2	8	0.156	0.157	1.25	1.25	1.37	266	266	240
					3×3×3	27	0.182	0.183	1.46	1.46	1.17	246	246	244
					4×4×4	64	0.179	0.179	1.44	1.44	1.30	248	248	227
					6×6×6	216	0.180	0.180	1.44	1.44	1.53	248	248	185
bcc-Nb	Nb	2.70	9.07	0.01	2×2×2	8	0.116	0.116	1.05	1.05	1.07	228	228	234
					3×3×3	27	0.138	0.138	1.25	1.25	1.01	210	210	204
					4×4×4	64	0.129	0.129	1.17	1.17	1.13	216	216	187
					6×6×6	216	0.131	0.131	1.19	1.19	1.27	215	215	154
				0.10	2×2×2	8	0.116	0.116	1.05	1.05	1.07	229	229	234
					3×3×3	27	0.138	0.138	1.25	1.25	1.01	209	209	204
					4×4×4	64	0.130	0.129	1.18	1.18	1.13	216	216	187
					6×6×6	216	0.132	0.131	1.20	1.20	1.27	214	214	154
fcc-Pd	Pd	2.66	2.65	0.01	2×2×2	8	0.135	0.135	0.36	0.36	0.35	198	198	74
					3×3×3	27	0.142	0.142	0.38	0.38	0.19	193	193	173
					4×4×4	64	0.140	0.144	0.37	0.37	0.25	194	194	156
					6×6×6	216	0.144	0.144	0.45	0.45	0.29	177	177	136
				0.10	2×2×2	8	0.134	0.135	0.36	0.36	0.35	199	199	74
					3×3×3	27	0.141	0.142	0.37	0.37	0.19	194	194	173
					4×4×4	64	0.143	0.144	0.38	0.38	0.25	192	192	156
					6×6×6	216	0.144	0.144	0.38	0.38	0.29	191	191	136
$A15$-V_3Si	V	2.23	11.37	0.01	1×1×1	8	0.203	0.203	2.30	2.32	5.31	234	235	128
					2×2×2	64	0.137	0.143	1.55	1.57	1.71	284	286	181
					3×3×3	216	0.147	0.145	1.68	1.69	1.42	274	275	204
				0.10	1×1×1	8	0.160	0.203	1.83	1.84	5.31	262	264	128
					2×2×2	64	0.139	0.143	1.58	1.60	1.71	282	283	181
					3×3×3	216	0.141	0.145	1.60	1.62	1.42	280	282	204
	Si	2.76	0.17	0.01	1×1×1	8	0.112	0.112	0.02			423		
					2×2×2	64	0.106	0.107	0.02			436		
					3×3×3	216	0.106	0.107	0.02			435		
				0.10	1×1×1	8	0.110	0.112	0.02			426		
					2×2×2	64	0.106	0.107	0.02			436		
					3×3×3	216	0.106	0.107	0.02			436		

DENSITY-FUNCTIONAL PERTURBATION THEORY PHONON CONVERGENCE

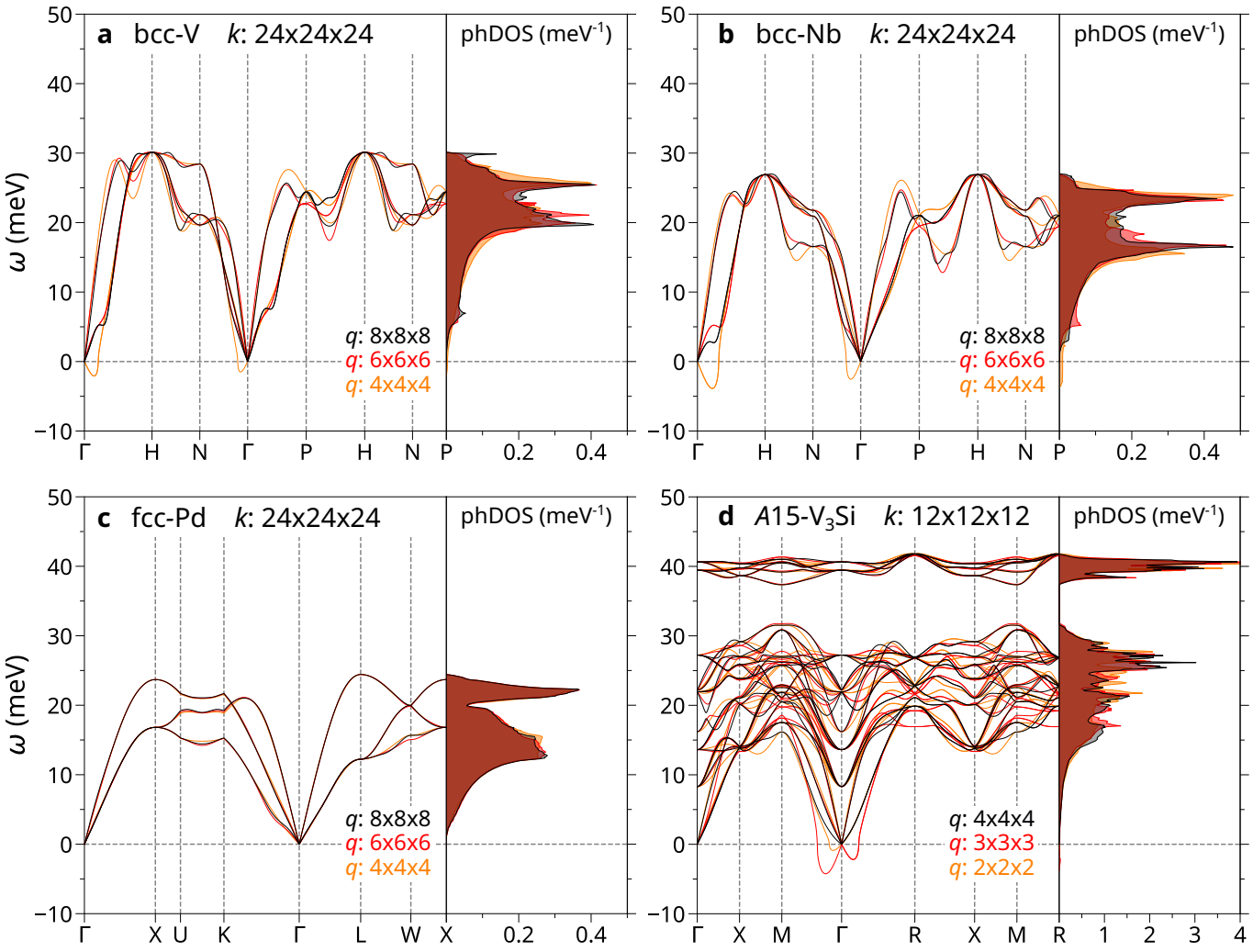

FIG. S4. **Convergence of phonon dispersion calculations with respect to *q*-point sampling.** Phonon dispersion relations for **a** bcc-V, **b** bcc-Nb, **c** fcc-Pd, and **d** *A*15-V_3Si. The uniform ***k***-point grid size for each material is specified at the top of the respective panels. Calculations were performed using density-functional perturbation theory (DFPT) with optimized norm-conserving Vanderbilt pseudopotentials (ONCVPSP). Parameters consistent with the rigid muffin-tin approximation (RMTA) electronic factor calculations were maintained. Different line colors (orange, red, and black) indicate increasing ***q***-point mesh density.

REFERENCES

[1] Gaspari, G. D. & Gyorffy, B. L. Electron-Phonon Interactions, d Resonances, and Superconductivity in Transition Metals. *Phys. Rev. Lett.* **28**, 801–805 (1972). URL https://link.aps.org/doi/10.1103/PhysRevLett.28.801.

[2] Evans, R., Gaspari, G. D. & Gyorffy, B. L. A simple theory of the electron-phonon mass enhancement in transition metals. *Journal of Physics F: Metal Physics* **3**, 39 (1973). URL https://dx.doi.org/10.1088/0305-4608/3/1/015.

[3] Pettifor, D. G. Theory of energy bands and related properties of 4d-transition metals. II. The electron-phonon matrix element, superconductivity and ion core enhancement. *Journal of Physics F: Metal Physics* **7**, 1009 (1977). URL https://dx.doi.org/10.1088/0305-4608/7/6/017.

[4] Jackson, J. D. *Classical Electrodynamics* (John Wiley & Sons, Nashville, TN, 1998), 3 edn.

[5] Gaunt, J. A. & Fowler, R. H. IV. The triplets of helium. *Philosophical Transactions of the Royal Society of London. Series A, Containing Papers of a Mathematical or Physical Character* **228**, 151–196 (1929). URL https://royalsocietypublishing.org/doi/abs/10.1098/rsta.1929.0004.

[6] Kleinman, L. & Bylander, D. M. Efficacious form for model pseudopotentials. *Phys. Rev. Lett.* **48**, 1425–1428 (1982). URL https://link.aps.org/doi/10.1103/PhysRevLett.48.1425.

[7] Bylander, D. M. & Kleinman, L. 4f resonances with norm-conserving pseudopotentials. *Phys. Rev. B* **41**, 907–912 (1990). URL https://link.aps.org/doi/10.1103/PhysRevB.41.907.

[8] Vanderbilt, D. Soft self-consistent pseudopotentials in a generalized eigenvalue formalism. *Phys. Rev. B* **41**, 7892–7895 (1990). URL https://link.aps.org/doi/10.1103/PhysRevB.41.7892.

[9] Hamann, D. R., Schlüter, M. & Chiang, C. Norm-conserving pseudopotentials. *Phys. Rev. Lett.* **43**, 1494–1497 (1979). URL https://link.aps.org/doi/10.1103/PhysRevLett.43.1494.

[10] Hamann, D. R. Optimized norm-conserving Vanderbilt pseudopotentials. *Phys. Rev. B* **88**, 085117 (2013). URL https://link.aps.org/doi/10.1103/PhysRevB.88.085117.

[11] Papaconstantopoulos, D. A. *et al.* Calculations of the superconducting properties of 32 metals with $Z \leq 49$. *Phys. Rev. B* **15**, 4221–4226 (1977). URL https://link.aps.org/doi/10.1103/PhysRevB.15.4221.

[12] Pickett, W. E. Transferability and the electron-phonon interaction: A reinterpretation of the rigid-muffin-tin approximation. *Phys. Rev. B* **25**, 745–754 (1982). URL https://link.aps.org/doi/10.1103/PhysRevB.25.745.

[13] Kortus, J., Mazin, I. I., Belashchenko, K. D., Antropov, V. P. & Boyer, L. L. Superconductivity of metallic boron in MgB_2. *Phys. Rev. Lett.* **86**, 4656–4659 (2001). URL https://link.aps.org/doi/10.1103/PhysRevLett.86.4656.

[14] Ginzburg, V. & Kirzhnits, D. On the problem of high temperature superconductivity. *Physics Reports* **4**, 343–356 (1972). URL https://www.sciencedirect.com/science/article/pii/0370157372900178.